


Cite this: *Nanoscale Adv.*, 2021, 3, 1029

# Tunable magnetothermal properties of cobalt-doped magnetite–carboxymethylcellulose ferrofluids: smart nanoplateforms for potential magnetic hyperthermia applications in cancer therapy†

Alice G. Leonel,<sup>a</sup> Alexandra A. P. Mansur,<sup>a</sup> Sandhra M. Carvalho,<sup>a</sup> Luis Eugenio F. Outon,<sup>b</sup> José Domingos Ardisson,<sup>c</sup> Klaus Krambrock<sup>b</sup> and Herman S. Mansur<sup>b</sup>  \*<sup>a</sup>

Magnetite nanoparticles are one of the most promising ferrofluids for hyperthermia applications due to the combination of unique physicochemical and magnetic properties. In this study, we designed and produced superparamagnetic ferrofluids composed of magnetite (Fe<sub>3</sub>O<sub>4</sub>, MION) and cobalt-doped magnetite (Co<sub>x</sub>-MION,  $x = 3, 5,$  and 10% mol of cobalt) nanoconjugates through an eco-friendly aqueous method using carboxymethylcellulose (CMC) as the biocompatible macromolecular ligand. The effect of the gradual increase of cobalt content in Fe<sub>3</sub>O<sub>4</sub> nanocolloids was investigated in-depth using XRD, XRF, XPS, FTIR, DLS, zeta potential, EMR, and VSM analyses. Additionally, the cytotoxicity of these nanoconjugates and their ability to cause cancer cell death through heat induction were evaluated by MTT assays *in vitro*. The results demonstrated that the progressive substitution of Co in the magnetite host material significantly affected the magnetic anisotropy properties of the ferrofluids. Therefore, Co-doped ferrite (Co<sub>x</sub>Fe<sub>(3-x)</sub>O<sub>4</sub>) nanoconjugates enhanced the cell-killing activities in magnetic hyperthermia experiments under alternating magnetic field performed with human brain cancer cells (U87). On the other hand, the Co-doping process retained the pristine inverse spinel crystalline structure of MIONs, and it has not significantly altered the average nanoparticle size ( $ca. \sim 7.1 \pm 1.6$  nm). Thus, the incorporation of cobalt into magnetite-polymer nanostructures may constitute a smart strategy for tuning their magnetothermal capability towards cancer therapy by heat generation.

Received 5th October 2020

Accepted 2nd January 2021

DOI: 10.1039/d0na00820f

rsc.li/nanoscale-advances

## 1. Introduction

Magnetic hyperthermia has currently received notable attention as a promising therapeutic approach to fight against cancer. It consists of using magnetic nanoparticles subjected to an alternating magnetic field (AMF) to induce heat release. The increase in the temperature of cells in the range of 41 °C to 45 °C, mainly

in cancer cells that are more sensitive than healthy cells, leads to thermal stress either at the cellular or molecular level, which results in apoptosis and necrosis.<sup>1–3</sup>

To date, chemotherapy, radiotherapy, and surgery are the standard procedures used for the treatment of malignant tumors. In particular, conventional chemotherapy makes use of drugs focused on killing cells without attaining specificity, which typically results in systemic toxicity and severe side-effects. Because hyperthermia is a non-invasive method, with localized nature, and consequently reduced adverse secondary effects, it can considerably improve the effectiveness of conventional treatments. Especially in cases of deep-seated cancers with restricted accessibility through traditional surgery, such as glioblastoma – the most lethal human brain tumor, magnetic hyperthermia has shown good prospects for treatment.<sup>2,4</sup>

Among a variety of magnetic nanomaterials that can be used in hyperthermia, iron oxide nanoparticles, particularly magnetite (Fe<sub>3</sub>O<sub>4</sub>), are the most attractive due to the combination of high saturation magnetization and reasonable magnetic

<sup>a</sup>Center of Nanoscience, Nanotechnology and Innovation – CeNano<sup>2</sup>I, Department of Metallurgical and Materials Engineering, Federal University of Minas Gerais – UFMG, Av. Antônio Carlos, 6627 – Belo Horizonte/MG, Brazil. E-mail: leonel.alice@gmail.com; alexandramansur.ufmg@gmail.com; sandhra.carvalho@gmail.com; hmansur@demet.ufmg.br

<sup>b</sup>Department of Physics, Federal University of Minas Gerais – UFMG, Av. Antônio Carlos, 6627 – Escola de Engenharia, Bloco 2 – Sala 2233, Belo Horizonte/MG, 31.270-901, Brazil. E-mail: hmansur@demet.ufmg.br; outon@fisica.ufmg.br; klauskrambrock@yahoo.com.br; Fax: +55-31-34091843; Tel: +55-31-34091843

<sup>c</sup>Centro de Desenvolvimento da Tecnologia Nuclear – CDTN, Av. Antônio Carlos, 6627 – Belo Horizonte, MG, Brazil. E-mail: jdr@cdtn.br

† Electronic supplementary information (ESI) available. See DOI: 10.1039/d0na00820f



anisotropy. These are some of the relevant variables that govern the heating capacity and the release of heat by the combination of Brownian and Néel relaxation processes of the nanocrystals.<sup>4–6</sup> Besides favorable magnetic performance, the nanoparticles must be biocompatible for biomedical applications. In this regard, the surface coating is essential not only to provide a high level of biocompatibility but also to regulate the colloidal stability of the nanoparticles, in reliance on surface charge and interfacial interactions, preventing agglomeration in physiological pH. Usually, surface coatings are achieved by chemical functionalization with shells of inorganic or organic ligands. Because the nature of these shells can influence the magnetic properties of nanomaterials, its choice should be carefully evaluated.<sup>6,7</sup>

Recently, natural polymers have gained much interest as stabilizing agents in colloidal chemistry towards biomedical applications owing to their biocompatibility, degradability, and non-toxicity. Carboxymethylcellulose (CMC), for example, is considered a cellulose derivative with enticing features for this purpose, such as natural abundance, low-cost, good chemical stability and versatility due to the presence of diverse functional groups accessible for chemical modification, and noteworthy water solubility in a wide range of pH.<sup>8–11</sup>

The magnetic properties of iron oxide nanoparticles can be remarkably changed by altering synthesis procedures, which affect their physicochemical characteristics, including size and its distribution, shape, composition, and structure. In particular, compositional tuning has attracted special attention as an efficient strategy to tailor the magnetic properties of spinel ferrite nanomaterials, which in specific cases can enhance hyperthermia ability.<sup>5,12</sup> For instance, the synthesis of cobalt doped magnetite nanoparticles by the partial replacement of Fe<sup>2+</sup> with Co<sup>2+</sup> species is a valuable approach to improve hyperthermia properties due to the increase in magneto-crystalline anisotropy of the system.<sup>12</sup> More interestingly, this effect can even be reached in nanoparticles with very small size, a condition that has good implications for biological application (*e.g.*, prolonged circulation time of nanoparticles in the blood), but on the other hand, not satisfactory for the heat generation.<sup>13,14</sup> In this regard, the thorough understanding of the variation in structure and magnetic properties of magnetite nanoparticles conjugated with polymer ligands as a function of progressive Co-doping is of great interest for scientific and technological perspectives, which has not been comprehensively explored yet.

Thus, in this study, we reported a *green* aqueous process using CMC as functional macromolecular capping ligand and extensive characterization of magnetite (MION) and cobalt-doped magnetite nanoconjugates, aiming at investigating the effect in the magnetic, physicochemical, and biological properties of the spinel ferrite ferrofluids. Additionally, magnetic hyperthermia experiments were performed *in vitro* with live glioblastoma cells to evaluate the influence of cobalt-doped magnetite nanoconjugates on inducing the death of malignant cancer cells through heat dissipation predominantly associated with relaxation mechanisms.

## 2. Experimental

### 2.1. Materials and cell cultures

Sodium carboxymethyl cellulose (CMC – degree of substitution DS = 0.7, product number: 419273, batch number: MKBR9194 V, average molecular mass  $M_w = 90$  kDa, viscosity 180 cps, 4% in H<sub>2</sub>O at 25 °C), iron(II) sulfate heptahydrate (FeSO<sub>4</sub>·7H<sub>2</sub>O, 99%), iron(III) chloride hexahydrate (FeCl<sub>3</sub>·6H<sub>2</sub>O, 97%), cobalt(II) acetate tetrahydrate (Co(CH<sub>3</sub>COO)<sub>2</sub>·4H<sub>2</sub>O, 98%), ammonium hydroxide (NH<sub>4</sub>OH, 28–30% NH<sub>3</sub> in H<sub>2</sub>O), 3-(4,5-dimethylthiazol-2-yl)-2,5-diphenyltetrazolium bromide (MTT, >98%), Triton™ X-100, hydrochloric acid (HCl, 37%), and sodium dodecyl sulfate (SDS, ≥99%) were supplied by Sigma-Aldrich (USA). Dulbecco's modified Eagle's medium (DMEM), Leibowitz medium (L-15), fetal bovine serum (FBS), phosphate-buffered saline (PBS), penicillin G sodium, amphotericin-b, streptomycin sulfate, and trypsin-DTA (0.5%) were purchased from Gibco BRL (USA). The previously mentioned chemicals were used without additional purification. Deionized (DI) water (Millipore Simplicity™) with a resistivity of 18 MΩ cm was used to prepare the solutions, and the procedures were carried out at room temperature unless specified in another way.

Human embryonic kidney cells (HEK 293T, American Type Culture Collection – ATCC@CRL 1573™) were provided by the Federal University of Minas Gerais (UFMG) as a model healthy cell line. Human glioma cells (U87) were obtained from Brazilian Cell Repository as a model cancer cell line (Banco de Células do Rio de Janeiro: BCRJ, Brazil; cell line authentication molecular technique, *Short Tandem Repeat (STR) DNA*; quality assurance based on the international standard NBR ISO/IEC 17025:2005).

### 2.2. Synthesis of MION and Co<sub>x</sub>-MION nanoparticles

The synthesis of colloidal Fe<sub>3</sub>O<sub>4</sub> nanoparticles (MION@CMC) and a series of cobalt doped iron oxide nanoparticles (Co<sub>x</sub>-MION@CMC  $x = 3, 5,$  and 10% mol of cobalt) was performed according to the coprecipitation method previously reported by our group<sup>15</sup> and described in detail in the ESI.†

### 2.3. Morphological, physicochemical, and magnetic characterization of MION and Co-MION nanoconjugates

Morphological characterization of the nanoparticles was acquired using a transmission electron microscope (TEM, Tecnai G2-20, FEI Company) at an accelerating voltage of 200 kV. Samples for TEM analyses were prepared by placing the colloidal suspensions onto carbon copper grids after dilution in deionized (DI) water (1:5 v/v, colloidal suspension: DI water) and ethanol (1:3 v/v, diluted colloidal suspension: ethanol). The average size of magnetic nanoparticles and their size-distribution were acquired based on the TEM images by measuring at least 100 nanoparticles selected at random using the DigitalMicrograph® image-processing program.

The crystal structures of nanoparticles were determined by X-ray diffraction (XRD) using PANalytical Empyrean diffractometer (Almelo, Netherlands) equipped with Cu-K $\alpha$  radiation ( $\lambda = 1.54056$  Å). The XRD patterns were recorded in the  $2\theta$  range



from 3.03 to 89.91° with a step scan of 0.06° s<sup>-1</sup>. Samples for XRD analyses were prepared by placing 2 mL of colloidal solutions onto plastic molds and drying at 40 ± 1 °C for 1 hour for the formation of the films.

The quantitative chemical analysis of cobalt content was performed by wavelength dispersive X-ray fluorescence spectrometry (WD-XRF) using a Supermini200 spectrometer (Rigaku Corporation, Tokyo, Japan). The Co *k*α line intensity was used to determine cobalt concentrations. The films were prepared as described for the XRD analyses.

X-ray photoelectron spectroscopy (XPS) measurements were performed using an Amicus spectrometer (Shimadzu) with a monochromatic Mg-Kα X-ray excitation source. Binding energies were corrected based on carbon 1 s signal (284.8 eV). The films were dried in a vacuum desiccator at room temperature for 1 hour and 30 min.

Fourier-transform infrared (FTIR) spectra were obtained by transmission technique (Thermo Fischer, Nicolet 670) from film samples in the wavenumber range from 400 to 4000 cm<sup>-1</sup> using 64 scans and a 2 cm<sup>-1</sup> resolution.

Dynamic light scattering (DLS) and zeta potential (ZP) measurements were performed using a ZetaPlus instrument (Brookhaven Instruments Corporation) with a laser light wavelength of 660 nm (35 mW red diode laser). The colloidal suspensions were diluted in filtered (0.45 μm aqueous syringe filter – Millex LCR 25 mm, Millipore) DI water (1:5 v/v, colloidal suspension: filtered DI water). All experiments were conducted at room temperature (25 ± 2 °C), and the light scattering was detected at 90°. At least ten measurements were obtained for each system, and the values were averaged.

Electron magnetic resonance (EMR) was carried out using a commercial X-band electron paramagnetic resonance spectrometer (Magnetech – Germany, model Miniscope MS400) operating at 9.44 GHz with a field modulation frequency of 100 kHz. A helium flux cryosystem (Oxford – England, model ESR 900) was used to change the temperature of the samples in the range from 77 to 300 K. The measurements were performed in colloidal suspensions with different concentrations (*C* = 0.1, 0.5, 1.0, and 5.0 mg mL<sup>-1</sup>). Also, all samples were tested in nanopowder form, which was dried inside borosilicate tubes at 120 °C (Wilma Labglass – USA).

Magnetic hysteresis curves *M*(*H*) were measured in the field range from -15 000 Oe to 15 000 Oe at 77 K and 300 K to determine the coercive field (*H*<sub>c</sub>) and saturation magnetization (*M*<sub>s</sub>). Zero-field cooling (ZFC) and field cooling (FC) curves were obtained using a vibrating sample magnetometer (VSM – model 7404, Lake Shore, USA) at 70 Oe in the temperature range from 77 K to 300 K. The following protocol was used for the measurements: the dried powder samples were cooled from 300 K to 77 K in zero applied field. Then, a field of 70 Oe was applied, and the magnetic moments were measured as the temperature was increased up to 300 K (ZFC curve). Subsequently, the sample was cooled down again to 77 K in the presence of the field (FC curve).

Magnetic hyperthermia experiments were performed using a Magnetherm™ instrument (Staffordshire, United Kingdom) with a solenoid diameter *D* = 50 mm and a number of turns *N* =

17. The magnetite suspensions with different concentrations (MION@CMC, *C* = 2.5, 5.0, and 20.0 mg mL<sup>-1</sup>) and Co-doped magnetite suspensions (Co<sub>x</sub>-MION@CMC, *C* = 2.5 mg mL<sup>-1</sup>) were exposed to an alternating magnetic field (AMF) with an amplitude of 19.9 kA m<sup>-1</sup> (250 Oe) and a frequency of 112.6 kHz for 30 min. The relative temperature increase values of the MION nanoconjugates and of the control samples (*i.e.*, water reference) were obtained by subtracting the initial temperature from the temperature measured at each time. In the sequence, the temperature increase of the water control was subtracted from that of the MION nanoconjugates, resulting in the “net” temperature (Δ*T*). The specific absorption rate (SAR, W g<sub>metal</sub><sup>-1</sup>) was estimated from the initial slope of the “net” temperature curve to consider the criterion of (quasi-)adiabatic conditions (linear fitting, *R*<sup>2</sup> ≥ 0.9999), using eqn (1).<sup>16</sup>

$$\text{SAR} = \frac{C\rho}{\phi} \frac{dT}{dt} \quad (1)$$

where *C* is the specific heat of the colloid, *ρ* is the density of the colloid, *φ* is the concentration of metal per mL of solution, and *dT/dt* represents the initial slope of the time-dependent temperature curve.

In the sequence, SAR values were normalized by the frequency (*f*) and field amplitude (*H*), obtaining intrinsic loss power (ILP, nH m<sup>2</sup> kg<sup>-1</sup>) according to eqn (2).<sup>16</sup>

$$\text{ILP} = \frac{\text{SAR}}{H^2 f} \quad (2)$$

#### 2.4. Biological characterization of MION and Co-MION nanoconjugates

The evaluation of cytotoxicity was performed using MTT (3-(4,5-dimethylthiazol-2-yl)-2,5-diphenyl tetrazolium bromide) experiments after the incubation of the nanoconjugates at different concentrations with human embryonic kidney cells (HEK 293T) and malignant glioma cells (U87) for 24 hours. The detailed protocol is described in the ESI.†

#### 2.5. Magnetic hyperthermia *in vitro* with glioma cancer cells

The magnetic hyperthermia experiments with human glioma cells (U87) were conducted according to the protocol specified in the ESI.† In brief, the cancer cells incubated with the magnetic nanoparticles samples (concentration = 15 μg mL<sup>-1</sup>) were exposed to the AMF (*H* = 19.9 kA m<sup>-1</sup> and frequency of 112.6 kHz) for 60 min (Magnetherm™, Staffordshire, United Kingdom). Next, the cells were washed, trypsinized, counted, and the percentage of cell viability was expressed concerning the live cells.

## 3. Results and discussion

### 3.1. Morphological, physicochemical, and magnetic characterization of MION and Co-MION nanoconjugates

TEM analysis was carried out to investigate the morphological features and sizes of the nanoconjugates, which are well-



recognized of pivotal relevance on their physicochemical and magnetic properties. TEM images indicated that magnetite and cobalt-doped magnetite nanoparticles were produced with predominant spherical morphology and an average size of  $7.1 \pm 1.6$  nm. As expected, due to the relatively moderate doping ratio (*i.e.*, <10 mol% of  $\text{Fe}^{2+}$ ), the incorporation of cobalt into  $\text{Fe}_3\text{O}_4$  nanoparticles did not alter their morphology and average size, as the nucleation and growth processes maintained similar kinetics during the synthesis. TEM images and histograms of the size distribution of MION@CMC and Co-doped MION nanoconjugates ( $\text{Co}_3\text{-MION@CMC}$  and  $\text{Co}_5\text{-MION@CMC}$ ) are presented in Fig. 1.

The XRD patterns (Fig. 2A) confirmed the formation of a single-phase inverse spinel structure of magnetite (JCPDS – 89-0691) for all samples, despite de Co-doping content. The peaks observed at  $30.1^\circ$ ,  $43.1^\circ$ ,  $35.5^\circ$ ,  $57.0^\circ$ , and  $62.6^\circ$  ( $2\theta$ ) correspond to the orientations along (220), (311), (400), (511) and (440) planes, respectively. There was no evidence of the formation of any other iron oxide phases. These XRD results demonstrated that the cobalt content had not changed the inverse spinel structure of  $\text{Fe}_3\text{O}_4$  (magnetite) nanoparticles. In addition, similarly, the increase in the cobalt doping concentration has not significantly altered the average nanocrystallite size of  $7.7 \pm 0.8$  nm estimated based on Scherrer's equation for all samples ( $\text{Co}_x\text{Fe}_{3-x}\text{O}_4$ ,  $x = 0, 0.03, 0.05$  and  $0.10$ ). These results are consistent with the average size measured by TEM for all nanoparticles (previous section) and are summarized in Table 1. Compared to the literature, upon Co-doping of iron oxide nanoparticles, some authors did not observe changes in crystallite size, independent of doping content, while others have detected significant changes. However, the observed changes in crystallite sizes were also followed by the variation in the diameter of nanoparticles resulting in monodomain nanostructures.<sup>13–18</sup> This trend was expected even considering potential residual stress in the nanomaterials caused by gradual partial substitution of  $\text{Fe}^{2+}$  species in the octahedral B sites of magnetite that possess an ionic radius ( $0.77 \text{ \AA}$ ) by  $\text{Co}^{2+}$  species with a smaller ionic radius ( $0.74 \text{ \AA}$ ) as the lattice parameters were quite similar for magnetite ( $8.3963 \text{ \AA}$ ) and cobalt ferrite ( $8.3919 \text{ \AA}$ ).<sup>13</sup> It should be noted that, according to the literature,<sup>17–19</sup> several aspects (*e.g.*, amorphous phases and nanoparticle size) can interfere in the resolution of XRD patterns and, therefore, on the precision of Scherrer's equation for directly measuring the average crystalline size of nanoparticles.<sup>20</sup> Nonetheless, the obtained nanoparticles represent a monodomain magnetic structure suitable for hyperthermia applications.

Further evidence of the incorporation of  $\text{Co}^{2+}$  species into magnetite nanoparticle structure by the partial replacement of  $\text{Fe}^{2+}$  ions in the nanocrystals was confirmed by WD-XRF. In Fig. 2B is presented the WD-XRF spectra of the Co-doped magnetite nanoparticles, where the  $\text{Co}_{10}\text{-MION@CMC}$  sample showed the peak located at  $2\theta = 52.8^\circ$  corresponding to the  $\text{Co-K}\alpha$  transition. Aiming at analyzing the doping of iron oxide nanoparticles with different Co content, the region of the spectra from  $45$  to  $55^\circ$  was enlarged and presented in Fig. 2C. As expected, a relative increase in the peak associated with  $\text{Co-K}\alpha$

transition was observed for higher cobalt content in the magnetite nanoparticles. It was also confirmed the appearance of the peak related to  $\text{Co-K}\beta$  transition, located at  $2\theta = 47.5^\circ$  in the high cobalt content sample ( $\text{Co}_{10}\text{-MION@CMC}$ ). The quantitative chemical analysis of Co by WD-XRF revealed concentrations of 0.8, 1.5, and 3.1% mol (related to total iron content) in the samples  $\text{Co}_3\text{-MION@CMC}$ ,  $\text{Co}_5\text{-MION@CMC}$ , and  $\text{Co}_{10}\text{-MION@CMC}$ , respectively. These results are in good consistency with the estimated theoretical percentages of 1.0, 1.7, and 3.3% (or equivalent to 3, 5, and 10% mol in relation to  $\text{Fe}^{2+}$ ) used in the synthesis of the nanocolloids.

Besides the bulk chemical composition, it is important to point out that surface features play a pivotal role in the properties of nanosized particles associated with their high surface to volume ratio as well as their stability as ferrofluids in aqueous media. Thus, XPS analyses were performed as an analytical technique for quantifying the chemical states of surface atoms. Fig. 3 shows the XPS spectra of MION@CMC (a) and  $\text{Co}_{10}\text{-MION@CMC}$  (d) obtained for Fe 2p (Fig. 3A) and Co 2p (Fig. 3B) regions. The XPS spectrum of MION@CMC (Fig. 3A) shows two sharp peaks at 710.4 eV ( $\text{Fe } 2p_{3/2}$ ) and 723.8 eV ( $\text{Fe } 2p_{1/2}$ ), which are associated with the Fe 2p transitions in magnetite. Moreover, the nonexistence of a satellite peak nearby 719 eV confirms the presence of both  $\text{Fe(II)}$  and  $\text{Fe(III)}$  species in the lattice.<sup>21–23</sup> The spin-orbit components ( $\text{Fe } 2p_{3/2}$  and  $\text{Fe } 2p_{1/2}$ ) are separated by a binding energy interval of approximately 13.4 eV. The XPS spectrum of  $\text{Co}_{10}\text{-MION@CMC}$  for the Fe 2p-region is similar to the same region of the MION@CMC sample. However, a slight decrease in the intensities of the peaks is observed, indicating a relative reduction in Fe content in the sample ascribed to the Co substitution.<sup>22</sup> The XPS spectrum of  $\text{Co}_{10}\text{-MION@CMC}$  (Fig. 3B(d)) shows two peaks at 781.1 eV ( $\text{Co } 2p_{3/2}$ ) and 797.1 eV ( $\text{Co } 2p_{1/2}$ ) associated with the Co 2p transitions in cobalt doped magnetite nanoparticles. Satellite peaks for  $\text{Co } 2p_{3/2}$  and  $\text{Co } 2p_{1/2}$  are also observed at 786.1 eV and 803.1 eV, respectively, where the first one is frequently used to confirm the presence of divalent cobalt.<sup>22</sup> Fig. 3C shows the comparative  $\text{Co } 2p_{3/2}$  XPS spectra of MION@CMC (a),  $\text{Co}_3\text{-MION@CMC}$  (b),  $\text{Co}_5\text{-MION@CMC}$  (c), and  $\text{Co}_{10}\text{-MION@CMC}$  (d). As the cobalt content increases,  $\text{Co } 2p_{3/2}$  peak becomes stronger and sharper,<sup>22</sup> which was well-correlated by linear regression (Fig. 3C, inset).

Moreover, bearing in mind the formation of colloidal ferrofluids composed of the MION core capped by the CMC ligand shell, it is appropriate to investigate the evolution of XPS spectra of C 1s and O 1s regions. For this analysis, in addition to MION@CMC and  $\text{Co}_{10}\text{-MION@CMC}$  samples, the CMC ligand was also evaluated. The XPS results are depicted in Fig. 4, and the peaks were identified *via* deconvolution of spectra fitted using the Gaussian function. The different chemical states of carbon (C–C/C–H, C–OH, O–C–O, and O=C–O) and oxygen (C–O/C–OH and C=O) assigned to the CMC polymer<sup>24</sup> were observed, and the binding energies (BE) associated with each bond are depicted in Table 2. The changes in the peak area distributions (Table 2) evidenced the occurrence of interactions between the functional groups of the polymer and metallic ions



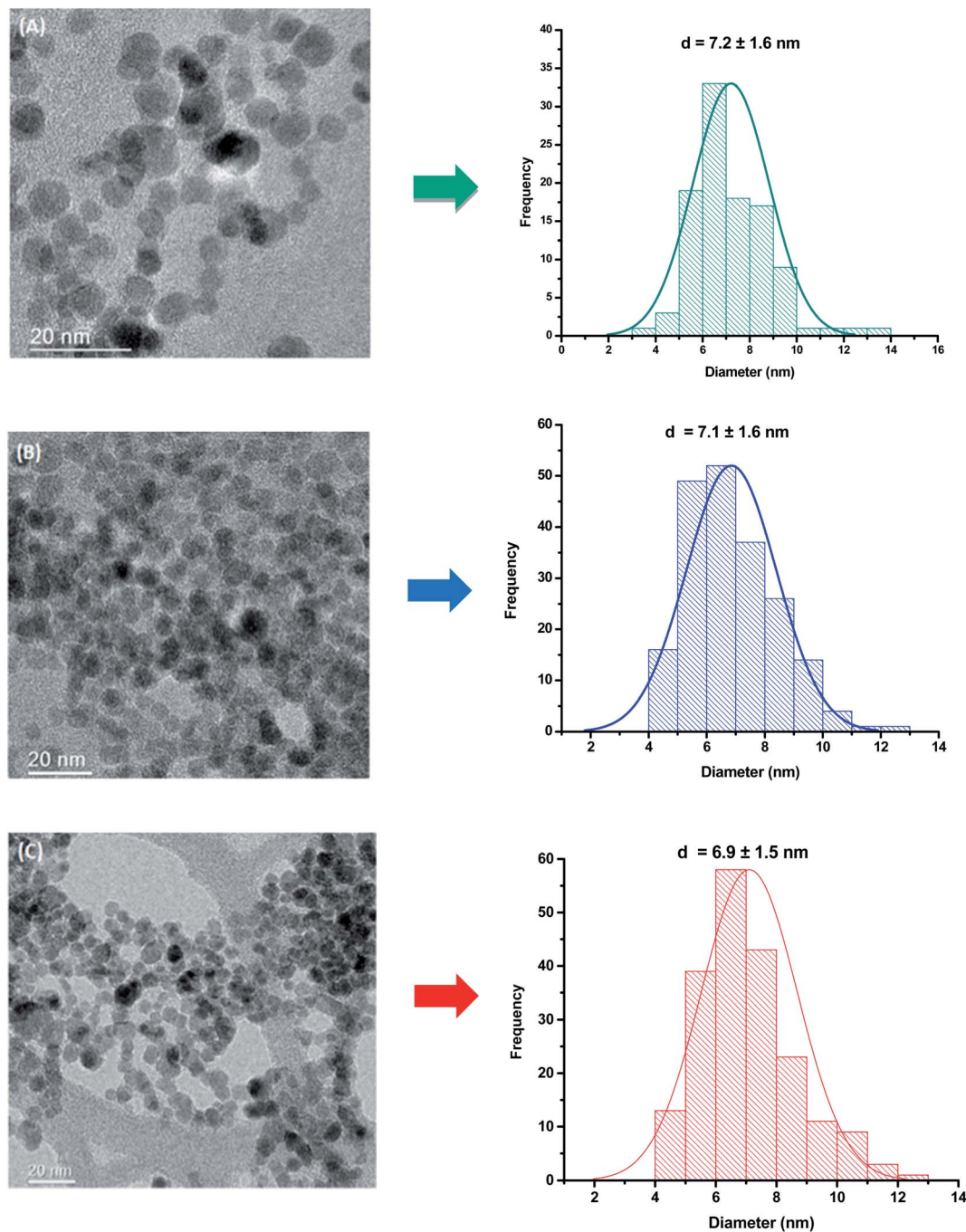


Fig. 1 TEM images and histogram of the size distribution of (A) MION@CMC, (B)  $\text{Co}_3$ -MION@CMC, and (C)  $\text{Co}_5$ -MION@CMC.

at the nanointerfaces,<sup>24</sup> which is also supported by the shift in BE ( $\Delta \sim 0.5$ ) of the band associated with C=O in O 1s.

The evaluation of the interactions developed at the interface between the functional groups of CMC ligand and the surfaces of the nanoparticles was carried out by FTIR spectroscopy. In Fig. 5A, it was observed in all spectra a broad band in the range from 3400 to 3200  $\text{cm}^{-1}$  assigned to  $\nu\text{O-H}$  vibrations, typically present in cellulose and derivatives such as CMC-based materials. Additionally, it was observed bands associated with asymmetric (1652 and 1590  $\text{cm}^{-1}$ ) and symmetric (1420 and

1320  $\text{cm}^{-1}$ ) stretches of  $\text{COO}^-$  groups as well as the band assigned to  $\nu\text{C}=\text{O}$  (1730  $\text{cm}^{-1}$ ), which are related to the carboxylic functionalities of CMC. The existence of two bands of symmetric and asymmetric carboxylates indicates two different types of coordination in polymer-metal complexes, according to the literature.<sup>15</sup> Thus, no noticeable changes were observed in the interactions at the interface of  $\text{Co}_x\text{Fe}_{3-x}\text{O}_4$  nanoparticle and CMC polymer by increasing the cobalt content. Moreover, vibrations from secondary alcohols ( $\nu\text{C2-OH}$ ; 1113  $\text{cm}^{-1}$ ;  $\nu\text{C3-OH}$ ; 1060  $\text{cm}^{-1}$ ) and the vibrational band related to the  $\beta\text{1-4}$



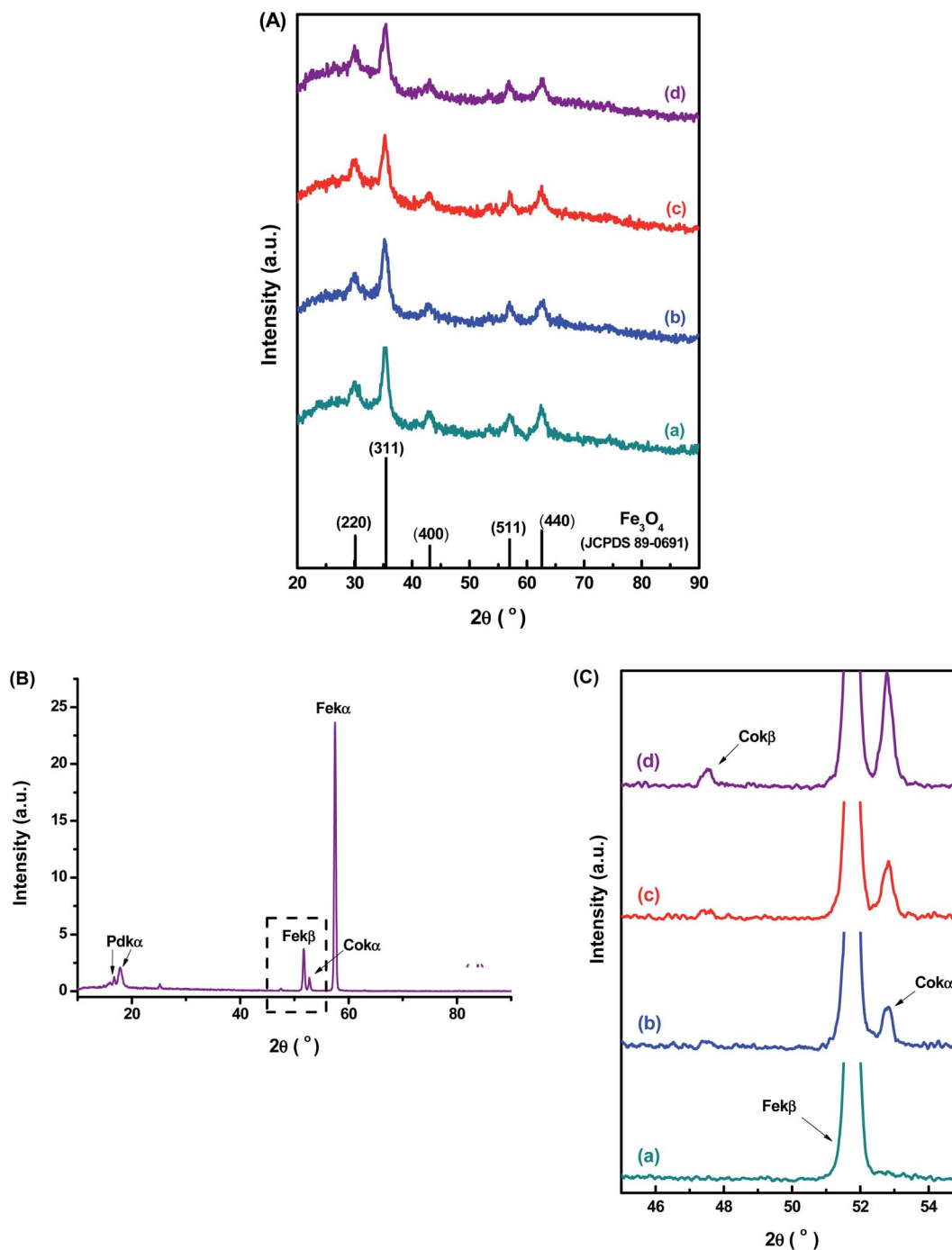


Fig. 2 (A) XRD patterns of (a) MION@CMC, (b) Co<sub>3</sub>-MION@CMC, (c) Co<sub>5</sub>-MION@CMC, and (d) Co<sub>10</sub>-MION@CMC samples compared with the reference pattern of Fe<sub>3</sub>O<sub>4</sub> (JCPDS – 89-0691). (B) WD-XRF spectra of Co<sub>10</sub>-MION@CMC. (C) Detail of the WD-XRF spectra region associated with the range of Co peaks for (a) MION@CMC, (b) Co<sub>3</sub>-MION@CMC, (c) Co<sub>5</sub>-MION@CMC, and (d) Co<sub>10</sub>-MION@CMC.

glycoside bonds at 890 cm<sup>-1</sup> were detected.<sup>8,25</sup> Furthermore, bands centered at 590 cm<sup>-1</sup> were assigned to stretching vibrations of tetrahedral group Fe–O and bands centered at 615–600 cm<sup>-1</sup> to νCo–O of the octahedral group (Fig. 5B).<sup>26–28</sup> In order to assess the effect of cobalt doping on Fe<sub>3</sub>O<sub>4</sub> nanoparticles, a semi-quantitative FTIR analysis was performed by considering the relative ratio of the areas of Co–O and Fe–O bands and the reference band (β1-4 glycoside bonds). The

results showed, as expected, a relative reduction of the Fe–O band and the increase in the Co–O band as the cobalt content increased (Fig. 5C).

A more detailed understanding of the physicochemical properties of the Co<sub>x</sub>-MION@CMC nanocolloids in the water medium was assessed by ZP and DLS analyses (Fig. 6). Regarding zeta potential (ZP), the results (~–60 mV) indicated that all nanoparticles were effectively stabilized by COO<sup>-</sup>



Table 1 Structural features of MION@CMC and Co-MION@CMC nanoparticles

Sample	Co content % mol (related to total iron content)		Crystallite size (nm)		Nanoparticle diameter – TEM (nm)
	Theoretical	XRF	(311)	(220)	
MION@CMC	0.0	0.0	8.1 ± 0.7	8.4 ± 0.7	7.2 ± 1.6
Co <sub>0.03</sub> Fe <sub>2.97</sub> O <sub>4</sub> (Co <sub>3</sub> -MION@CMC)	1.0	0.8	6.1 ± 0.1	8.4 ± 0.4	7.1 ± 1.6
Co <sub>0.05</sub> Fe <sub>2.95</sub> O <sub>4</sub> (Co <sub>5</sub> -MION@CMC)	1.7	1.5	7.6 ± 0.4	7.3 ± 0.5	6.9 ± 1.5
Co <sub>0.1</sub> Fe <sub>2.9</sub> O <sub>4</sub> (Co <sub>10</sub> -MION@CMC)	3.3	3.1	8.3 ± 0.8	7.5 ± 0.7	7.1 ± 1.6

groups, independent of the Co concentration investigated, mostly by electrostatic repulsion ( $ZP < -30$  mV).<sup>15,25</sup> Based on DLS studies, the average relative size of MION and Co-doped MION inorganic core combined with the CMC coating uniformly dispersed and stabilized in aqueous solution, referred to as hydrodynamic diameter ( $H_D$ ). Hydrodynamic diameter is affected by the overall balance of ionic strength of the medium and polymer conformation structure due to water solvation, excluded volume, hydrophobic interactions, and electrostatic repulsion/attraction between ionic sites.<sup>29–31</sup> In this sense, as CMC is a pH-sensitive polymer, which above its pKa ( $\sim 4.3$ ),<sup>25</sup> both pH ( $6.5 \pm 0.5$ ) and conductivity ( $420 \pm 10$   $\mu$ S) of ferrofluids were maintained constant for DLS measurements.

Thus, under these conditions, the average  $H_D$  values varied between 46 and 74 nm with a reduction of the size observed for Co-doped ferrofluids. This trend was ascribed to the stronger interactions of Co<sup>2+</sup> with CMC functional groups (*i.e.*, –COOH, –OH) supported by the XPS results in the previous section, rendering conformational changes of the overall colloidal nanostructures.

According to the literature,<sup>32</sup> the heat dissipation in single-domain magnetic nanoparticles is caused by the combination of Néel and Brownian relaxation of the magnetic moments. The dominant mechanism is governed not only by the nanoparticle size but also by its composition, shape, and medium viscosity. Thus, there are several approaches to tune relaxation times and,

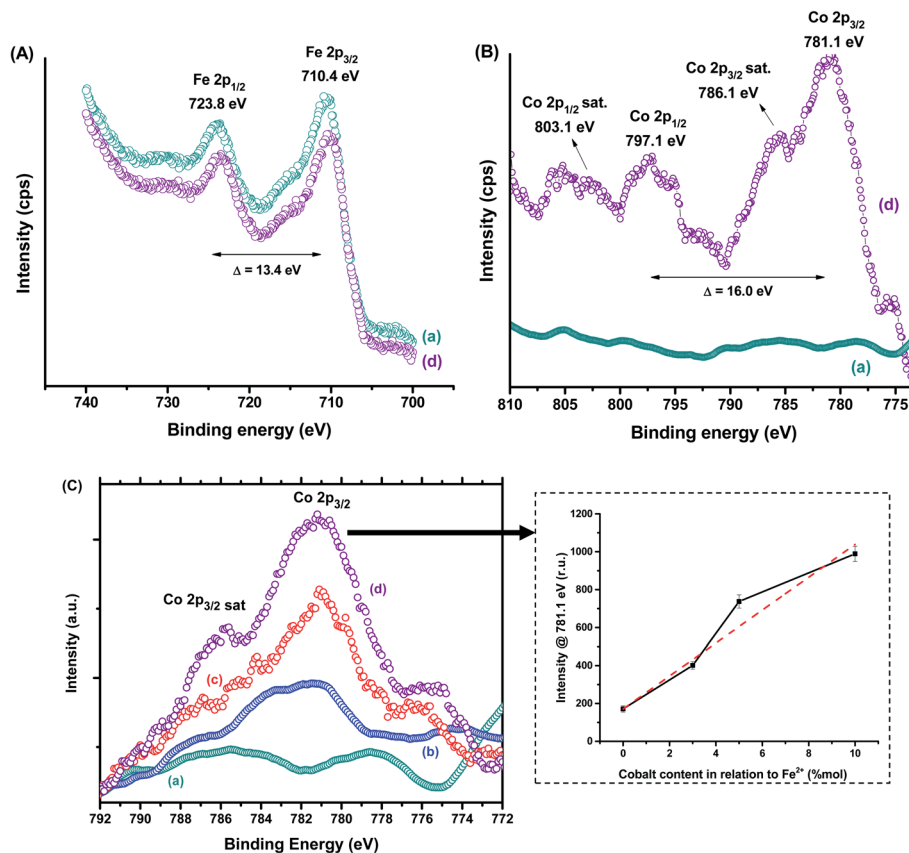


Fig. 3 XPS spectra of (A) Fe 2p and (B) Co 2p regions for (a) MION@CMC and (d) Co<sub>10</sub>-MION@CMC. (C) Spectra of Co 2p<sub>3/2</sub> region for (a) MION@CMC, (b) Co<sub>3</sub>-MION@CMC, (c) Co<sub>5</sub>-MION@CMC, and (d) Co<sub>10</sub>-MION@CMC. Inset: evolution of intensity at Co 2p<sub>3/2</sub> peak with increasing cobalt content.



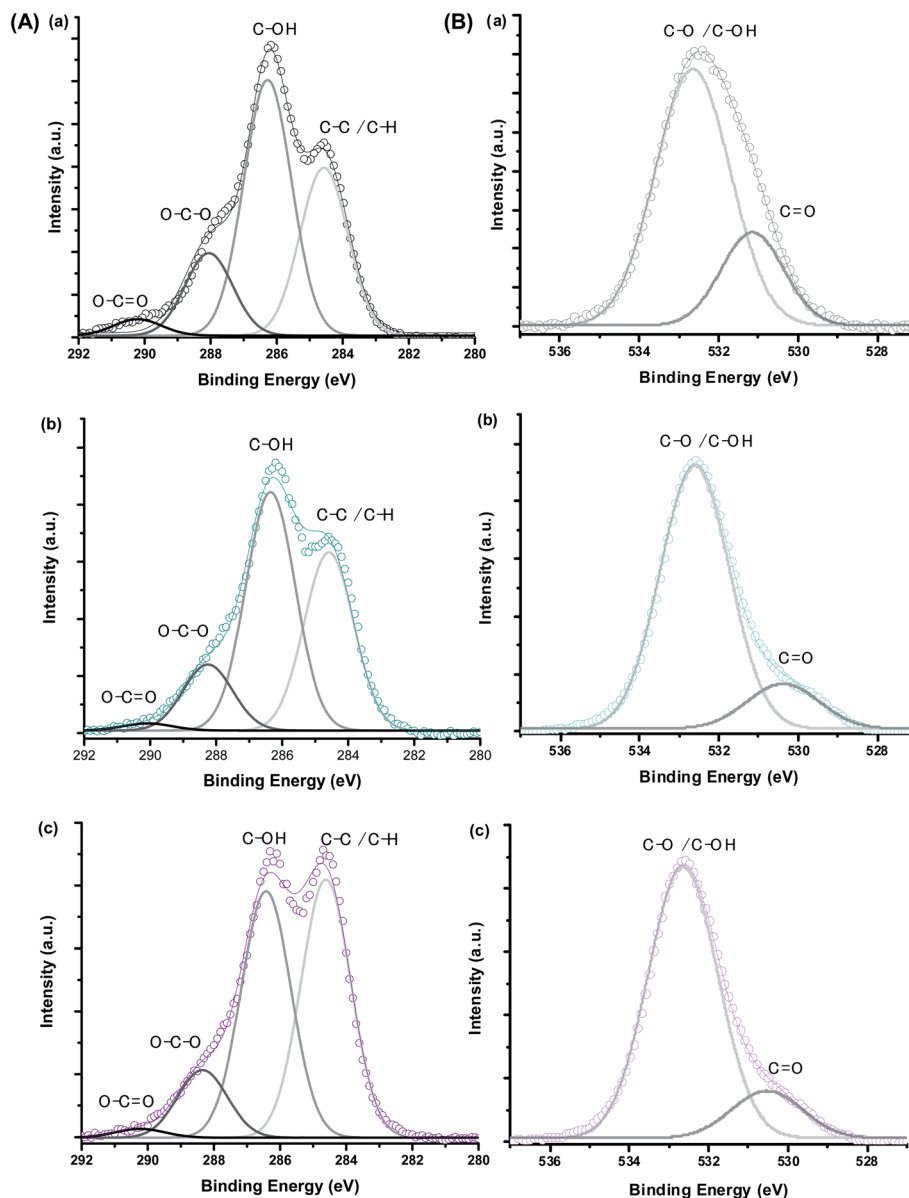


Fig. 4 XPS spectra of (A) C 1s and (B) O 1s regions obtained for (a) CMC ligand, (b) MION@CMC, and (c) Co<sub>10</sub>-MION@CMC.

therefore, the nanoparticle relaxation behavior.<sup>32</sup> Some comprehensive reviews and elegant studies<sup>33,34</sup> have reported that the Brownian rotation can be the most important

mechanism for magnetic relaxation of nanoparticles with large magnetic anisotropy, such as Co-ferrite nanoparticles. In this case, the hydrodynamic diameter is a critical parameter to

Table 2 Binding energies and relative peak area ratios for C 1s and O 1s

Peak assignment	CMC		MION@CMC		Co <sub>10</sub> -MION@CMC	
	BE (eV) ± 0.2	Peak area ratio (%)	BE (eV)	Peak area ratio (%)	BE (eV)	Peak area ratio (%)
C 1s – C–C/C–H	284.6	32	284.6	36	284.6	45
C 1s – C–OH	286.3	49	286.4	49	286.4	42
C 1s – O–C–O	288.1	16	288.3	14	288.3	12
C 1s – O–C=O	290.2	3	290.1	1	290.2	1
O 1s – C–O/C–OH	532.6	77	532.6	85	532.6	85
O 1s – C=O	531.1	23	530.4	15	530.5	15





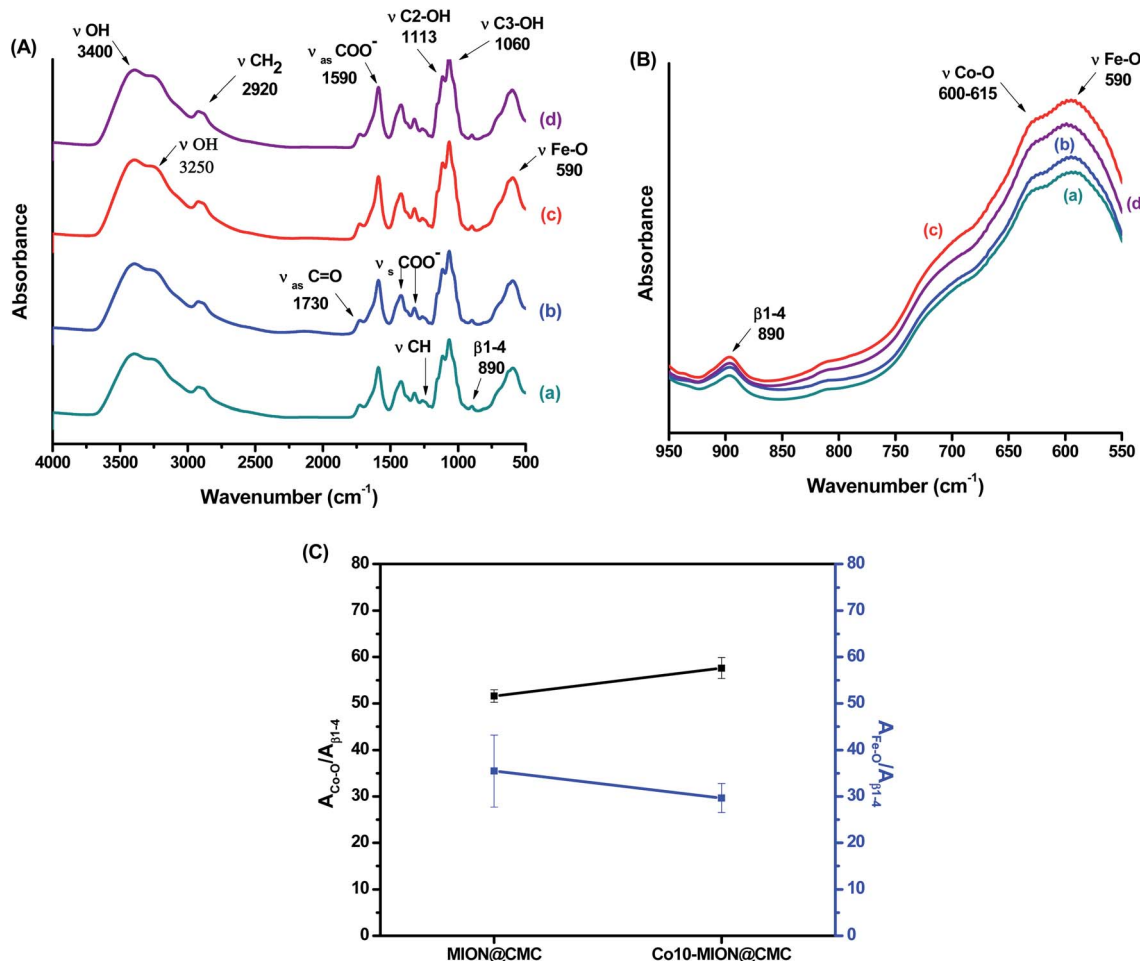


Fig. 5 (A) FTIR spectra of (a) MION@CMC, (b) Co<sub>3</sub>-MION@CMC, (c) Co<sub>5</sub>-MION@CMC and (d) Co<sub>10</sub>-MION@CMC. (B) Detail of the FTIR spectra region associated with the range of  $\beta 1-4$ , Fe-O and Co-O vibrations. (C) Evolution of Fe-O and Co-O bands due to cobalt doping.

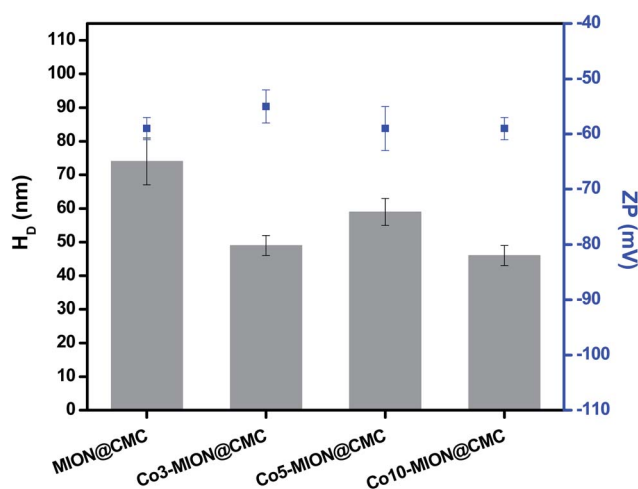


Fig. 6 DLS and ZP results obtained from MION@CMC and Co<sub>x</sub>-MION@CMC at pH = 6.5 ± 0.5 and conductivity = 420 ± 10  $\mu\text{S}$  ( $n \geq 10$ ; mean ± standard deviation, SD).

determine the power absorption in magnetic hyperthermia. Thus, the reduction in  $H_D$  of the Co-MION samples could minimize the effect of CMC coating in reducing the thermal responses.<sup>35</sup> Consequently, the impact of increasing the magnetic anisotropy by adding a more anisotropic cation (cobalt) can be overcome, favoring the heat generation.<sup>36</sup>

The magnetic properties of nanoconjugates were investigated by electron magnetic resonance (EMR) spectroscopy and vibrating sample magnetometry (VSM). Fig. 7A shows the typical EMR signals measured at room temperature ( $T = 300$  K) for samples in powder form. These EMR spectra are typical of superparamagnetic nanoferrites.<sup>37</sup> However, a progressive transition from superparamagnetic to ferrimagnetic behavior with increasing cobalt content is observed. This trend is attributed to the increasing magnetocrystalline anisotropy of magnetite nanoparticles through Co incorporation.<sup>38</sup> Fig. 7B shows EMR spectra also measured at room temperature for ferrofluids (concentration of magnetic nanoparticles = 1.0 mg mL<sup>-1</sup>). Similarly, the superparamagnetic behavior was evidenced by the resonance lines, which were shifted to lower fields, became broader and more anisotropic as the cobalt content increased.<sup>15</sup> It was verified, therefore, the same trend



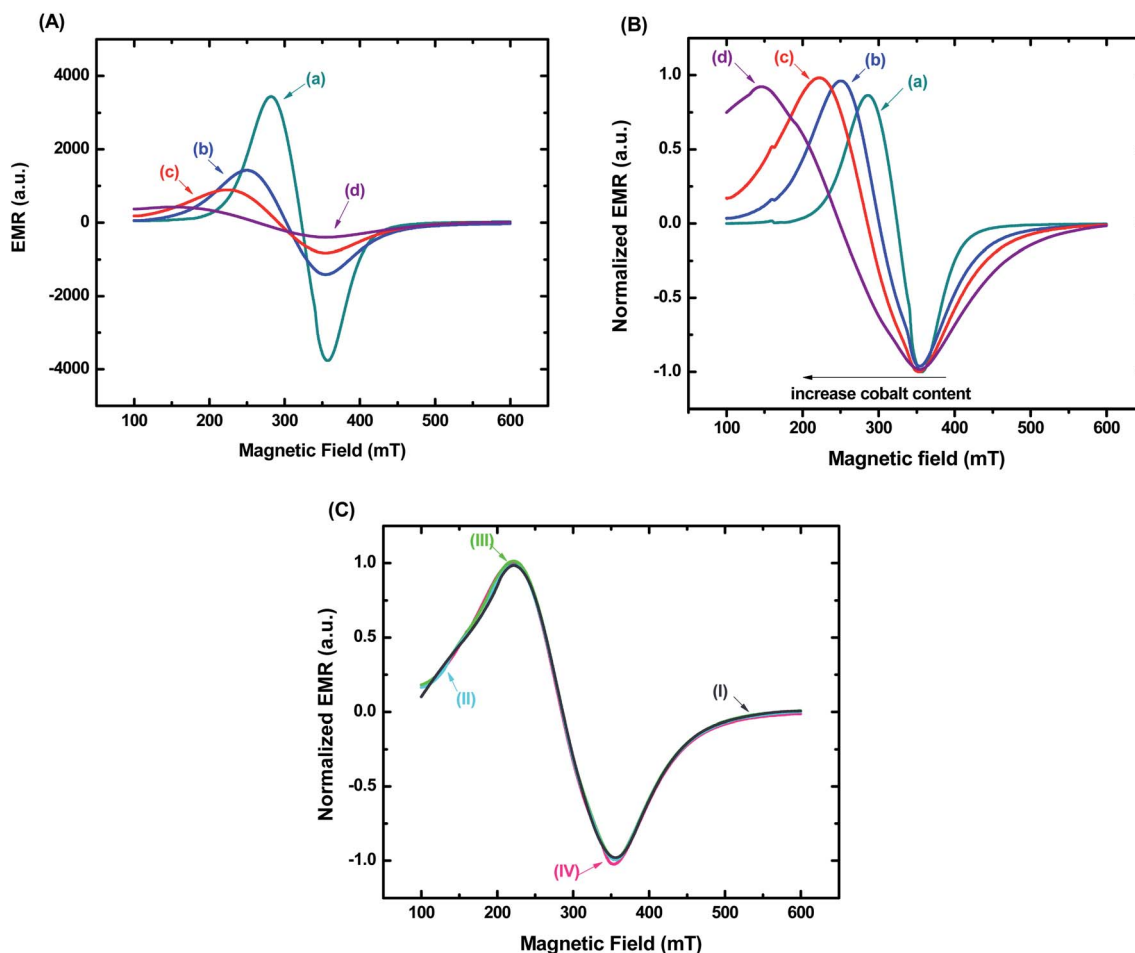


Fig. 7 EMR spectra of (a) MION@CMC, (b) Co<sub>3</sub>-MION@CMC, (c) Co<sub>5</sub>-MION@CMC, and (d) Co<sub>10</sub>-MION@CMC for (A) samples in powder form and (B) ferrofluids. (C) EMR spectra of Co<sub>5</sub>-MION@CMC ferrofluids with (I) 0.1 mg mL<sup>-1</sup>, (II) 0.5 mg mL<sup>-1</sup>, (III) 1.0 mg mL<sup>-1</sup> and (IV) 5.0 mg mL<sup>-1</sup>.

for both sample nature. However, considering biological applications, it is highly desirable to use ferrofluids due to their colloidal stability driven by the balance between attractive and repulsive interactions, which hamper agglomeration and reduce the risks of embolism.<sup>32,39</sup> It is important to highlight that besides the Van der Waal's attractive forces, another primary interaction that is attractive in nature and can occur between magnetic nanoparticles in suspension is the dipolar interactions. They become important to the magnetic properties of the nanocolloids, especially when the concentration of ferrofluids increases.<sup>32,40</sup> Thus, to evaluate the relevance of magnetic dipolar forces in our systems, EMR analyses were performed in Co<sub>5</sub>-MION@CMC suspensions with concentrations varying in the range from 0.1 mg mL<sup>-1</sup> to 5.0 mg mL<sup>-1</sup>. These values were chosen based on EMR and hyperthermia studies reported in the literature.<sup>2,41,42</sup> It was observed no difference in the EMR spectra for all the concentrations evaluated (Fig. 7C), which evidenced the absence of interparticle interactions even with a 50-fold variation in concentration. From a colloidal chemistry perspective, this result can be explained in terms of the presence of long-chained CMC ligand shell forming the nanoconjugates, contributing to the

electrostatic/steric repulsion and, therefore, leading to the ferrofluid stability.<sup>15,32</sup> This magnetic behavior corroborated the DLS and ZP results presented in the previous sections.

The superparamagnetic behavior of all samples was confirmed by hysteresis curves measured at 301 K and 77 K as a function of the magnetic field. In Fig. 8A, it was observed the absence of hysteresis loops at room temperature, which means that magnetization becomes zero when the external field is removed. In this case, the nanoparticles are in the superparamagnetic regime, characterized by the complete reversibility of the magnetization process. At lower temperatures, however, some particles are blocked, and their magnetization is aligned along the field direction, revealing ferrimagnetic behavior. If the field is removed, the material will not reach zero magnetization unless a coercive field is applied. Accordingly, hysteresis loops are observed (Fig. 8B). Considering that the substitution of Fe<sup>2+</sup> with Co<sup>2+</sup> species increase the magnetocrystalline anisotropy of magnetite nanoparticles, it is expected the higher coercive field to reverse the magnetization of the Co-MION nanoconjugates. In this sense, as the cobalt content increase, stronger hysteresis was observed at 77 K, consistent with the literature.<sup>38,43</sup> Saturation magnetization ( $M_s$ ) property



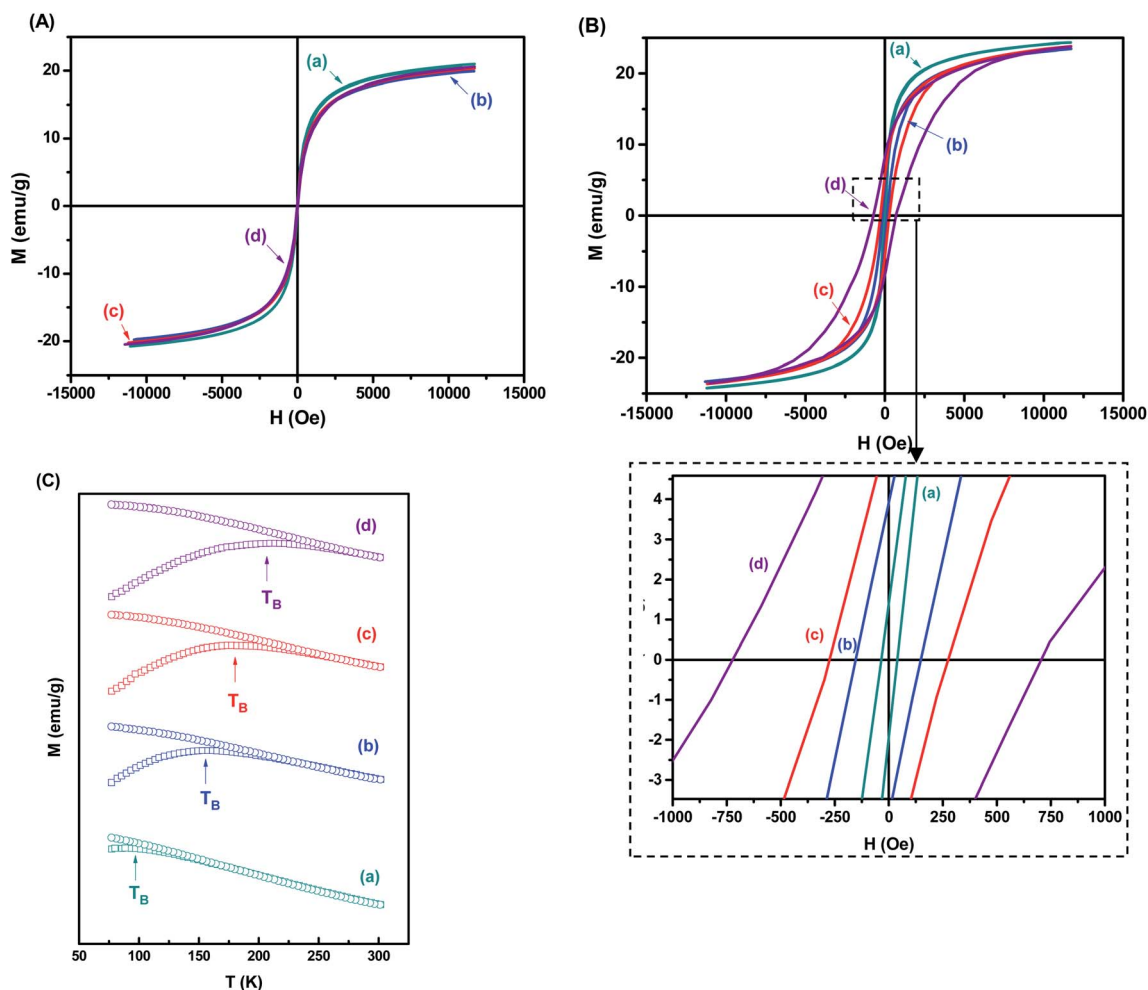


Fig. 8 Hysteresis curves measured at (A) 301 K and (B) 77 K for (a) MION@CMC, (b) Co<sub>3</sub>-MION@CMC, (c) Co<sub>5</sub>-MION@CMC, and (d) Co<sub>10</sub>-MION@CMC. (C) Magnetization curves in the temperature range from 301 K to 77 K for zero-field cooling (ZFC) and after applying a field of 70 Oe for field cooling (FC).

was similar for all samples ( $\sim 19\text{--}25\text{ emu g}^{-1}$ ) at low and room temperatures based on hysteresis curves. This is in agreement with the literature where  $M_s$  values of doped nanoparticles were comparable to Fe<sub>3</sub>O<sub>4</sub> with similar size.<sup>14</sup> The curves at 77 K also indicated the expected increase of coercivity ( $H_C$ ) considering the Co<sup>2+</sup> content added to the samples, considering that higher values of  $H_C$  were generally associated with highly anisotropic systems.<sup>13</sup>

Fig. 8C shows the temperature dependence of the zero-field cooling magnetization curve for the nanocolloids. As the temperature increases, the magnetization shows a maximum value defined as the blocking temperature ( $T_B$ ). It is determined by the competition between the aligning field and the disordering effects induced by the thermal agitation. Above  $T_B$ , the superparamagnetic state is achieved, allowing the spin relaxation. The main factor that determines the superparamagnetic properties of monodomain nanocrystals is the magnetocrystalline anisotropy, which serves as an energy barrier to block the spin relaxation, and it originates principally from the spin-orbital coupling of magnetic ions at crystal lattice sites.<sup>43,44</sup>

According to Fig. 8C, the blocking temperature of the nanocolloids increases as the cobalt content increases. This can be explained by the stronger orbital-spin coupling at Co<sup>2+</sup> lattice compared to Fe<sup>2+</sup>, which results in much higher anisotropy barriers in Co-doped magnetite nanocrystals and consequently higher  $T_B$ .<sup>19,45</sup>

Bearing in mind the biomedical applications of these ferrofluids, the heating efficiency of the nanocolloids was investigated by magnetic hyperthermia analyses. Our approach in this study has been focused on the heating ability related to the nanoparticle concentration and cobalt content. Thus, firstly we analyzed the variation in temperature over time of the MION colloids with different concentrations ( $C = 2.5, 5.0,$  and  $20.0\text{ mg mL}^{-1}$ ) exposed to an alternating magnetic field ( $H = 19.9\text{ kA m}^{-1}$  and frequency ( $f = 112.6\text{ kHz}$ ) for 30 min (Fig. S1 – ESI†). At this point, it is important to highlight that the  $Hf$  value obtained at these conditions ( $2.2 \times 10^9\text{ A m}^{-1}\text{ s}^{-1}$ ) is lower than the recommended limit dose of  $5 \times 10^9\text{ A m}^{-1}\text{ s}^{-1}$ , considering the safety of the patient under therapy avoiding uncontrolled



heating of tissue caused by the induction of eddy currents and peripheral muscles stimulation.<sup>13,14</sup>

As expected, the increase in the concentration of magnetic nanoparticles evidenced the enhancement of the ferrofluid temperature likely due to the magnetic dipolar interactions, which became more pronounced as the mean inter-particle distance was reduced.<sup>32</sup> Subsequently, in Fig. 9 is presented the changes in the net temperature over time (A) and the specific absorption rate (SAR) values (B, left-axis) of the nanocolloids ( $C = 2.5 \text{ mg mL}^{-1}$ ) when they were exposed to the AMF for 30 min. As the cobalt content was increased, the SAR values also improved, with a significant change was observed upon small doping concentration ( $x = 0.03$ ). It is well stated in the literature the increase of SAR parameter upon Co-doping up to values of  $x = 0.6\%$ .<sup>13,14</sup> This result was presumed, considering that the replacement of  $\text{Fe}^{2+}$  by  $\text{Co}^{2+}$  increases the magneto-crystalline anisotropy of the system, which is an efficient strategy to improve hyperthermia properties of the magnetite nanoparticles.<sup>12</sup> The increase in SAR values followed the same trend observed for the coercive field at low temperature as both parameters are associated with magnetic anisotropy of the systems (Fig. 9B, right-axis).<sup>13,14</sup>

Since SAR describes the efficiency of heat conversion, it is an important parameter for cancer nanomedicine from which one can determine the dosages applied to a tumor to achieve a reliable inactivation of target cells. For (nano)materials with high SAR values, it is possible to reduce the relative dose applied to the patient to a minimum level.<sup>46</sup> Table 3 summarizes the heating efficiency (SAR) and ILP of some superparamagnetic ferrite-based nanoparticles reported in the literature in comparison to the values obtained in this study.

SAR values vary significantly among the different works, as previously reported in the literature.<sup>47</sup> It is difficult to make a direct comparison between these results owing to a wide variety of conditions that can influence SAR and ILP values. Considering superparamagnetic particles, the SAR is highly influenced by the frequency and strength of the magnetic field. It is also dependent on the relaxation time of the nanoparticles in colloidal suspensions, which in turn is governed by the

intrinsic size and anisotropy of the nanoparticles as well as the hydrodynamic size and solution viscosity.<sup>18</sup> Thus, for the cases showed here, the combination of different parameters, such as chemical composition, size, surface coating, concentration (that may change dipolar interactions), and field characteristics affected these values, being responsible for enhancing or diminishing the heating efficiency of nanoparticles. Although ILP values are independent of the magnetic field parameters, this parameter still relies on the key features of the magnetic nanoparticles, and therefore they can vary significantly.

### 3.2. Biological characterization of MION and Co-MION nanoconjugates

Mitochondria activity assays (*i.e.*, MTT) were performed to evaluate the cytotoxicity of MION@CMC and Co-MION@CMC at different concentrations (1.0, 3.0, and  $10.0 \mu\text{g mL}^{-1}$ ) for 24 h on HEK 293T healthy cells (Fig. 10A) and glioblastoma U87 cancer cells (Fig. 10B).

The results evidenced a reduction of cell viability responses by increasing the concentration of nanocolloids for both cell types, demonstrating that cell viability is concentration-dependent. According to the international standard ISO 10933-5, the cell viability response lower than 70% indicates a cytotoxic behavior of the material under evaluation. Thus, for concentrations higher than  $3.0 \mu\text{g mL}^{-1}$ , the MION@CMC and Co-doped nanoconjugates showed crescent cytotoxic by increasing the concentration. These findings are very relevant as several reports inaccurately sustain that iron oxide nanoparticles are non-toxic, which is not necessarily valid.<sup>11,15,49</sup> The cytotoxicity response of iron oxide nanoparticles (IONs) will depend on the amalgamation of several aspects, including concentration, chemical composition, size, morphology, surface area, capping ligands, as well as cell type and biological toxicity protocol.<sup>11,15,49</sup> To this end, the cytotoxicity of IONs should be properly addressed and cannot be neglected. Although for use as a contrast agent, the cytotoxicity of MION-based nanoconjugates can be a limitation, for cancer therapy, it is certainly a major advantage. Therefore, a compromise of both aspects must be properly well-adjusted for each specific application.

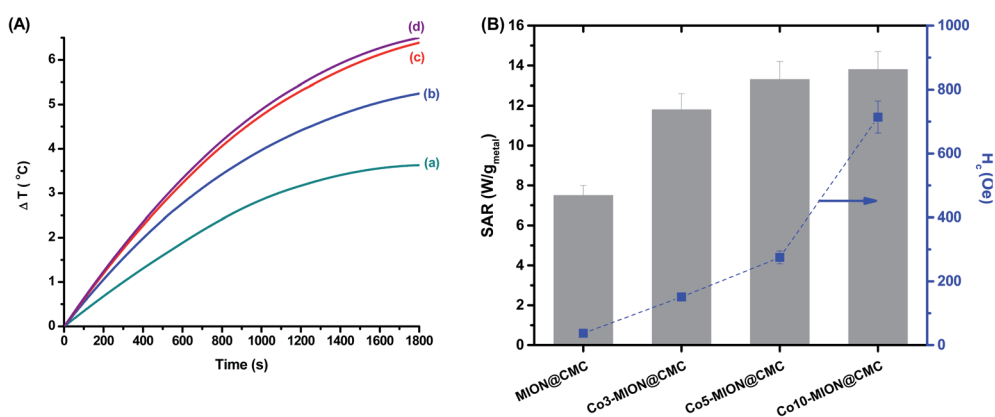


Fig. 9 (A) Variation in "net" temperature over time for (a) MION@CMC, (b) Co<sub>3</sub>-MION@CMC, (c) Co<sub>5</sub>-MION@CMC, and (d) Co<sub>10</sub>-MION@CMC. (B) SAR values in comparison to the coercive field of nanoconjugates at low temperature.



Table 3 Parameters of magnetic nanoparticles and SAR/ILP values from literature compared to the obtained in this work

Magnetic nanomaterial	Concentration	Size (nm)	Coating	$H$ (kA m <sup>-1</sup> )	$f$ (kHz)	SAR (W g <sub>metal</sub> <sup>-1</sup> )	ILP (nH m <sup>2</sup> kg <sup>-1</sup> )	Ref.
Fe <sub>3</sub> O <sub>4</sub>	1.6% w/w	8	Oleic acid oleylamine	12	183	6.5 ± 0.5	0.25 <sup>a</sup>	13
Co <sub>0.2</sub> Fe <sub>2.8</sub> O <sub>4</sub>	1.6% w/w	8	Oleic acid oleylamine 1,2-hexadecanediol	12	183	11.2 ± 1.0	0.43 <sup>a</sup>	
CoFe <sub>3</sub> O <sub>4</sub>	1.5% w/w	8	Oleylamine	12	183	10.8 ± 1.9	0.41 <sup>a</sup>	
Co <sub>0.2</sub> Fe <sub>2.8</sub> O <sub>4</sub>	5.0 mg mL <sup>-1</sup>	30	—	24	419	~15	~0.06 <sup>a</sup>	14
					542	~30	~0.10 <sup>a</sup>	
nanomag®-D-sprio	5.0 mg mL <sup>-1</sup>	—	Dextran	20	150	26 ± 1	0.43 <sup>a</sup>	47
Fe <sub>3</sub> O <sub>4</sub>	50 mg mL <sup>-1</sup>	6–12	Sodium oleate	15.9	62	14	0.89	48
Fe <sub>3</sub> O <sub>4</sub>	58 mg mL <sup>-1</sup>	8	—	23.8	100	52.8	0.93	
				9.5	100	17.2	1.89	
Fe <sub>3</sub> O <sub>4</sub> (MION@CMC)	2.5 mg mL <sup>-1</sup>	7	CMC	19.9	112.6	7.5 ± 0.5	0.17 ± 0.01	This work
Co <sub>0.03</sub> Fe <sub>2.97</sub> O <sub>4</sub> (Co <sub>3</sub> -MION@CMC)						11.8 ± 0.8	0.26 ± 0.02	
Co <sub>0.05</sub> Fe <sub>2.95</sub> O <sub>4</sub> (Co <sub>5</sub> -MION@CMC)						13.3 ± 0.9	0.29 ± 0.02	
Co <sub>0.1</sub> Fe <sub>2.9</sub> O <sub>4</sub> (Co <sub>10</sub> -MION@CMC)						13.8 ± 0.9	0.31 ± 0.02	

<sup>a</sup> Calculated parameters based on the SAR,  $H$ , and  $f$  values extracted from respective references cited.

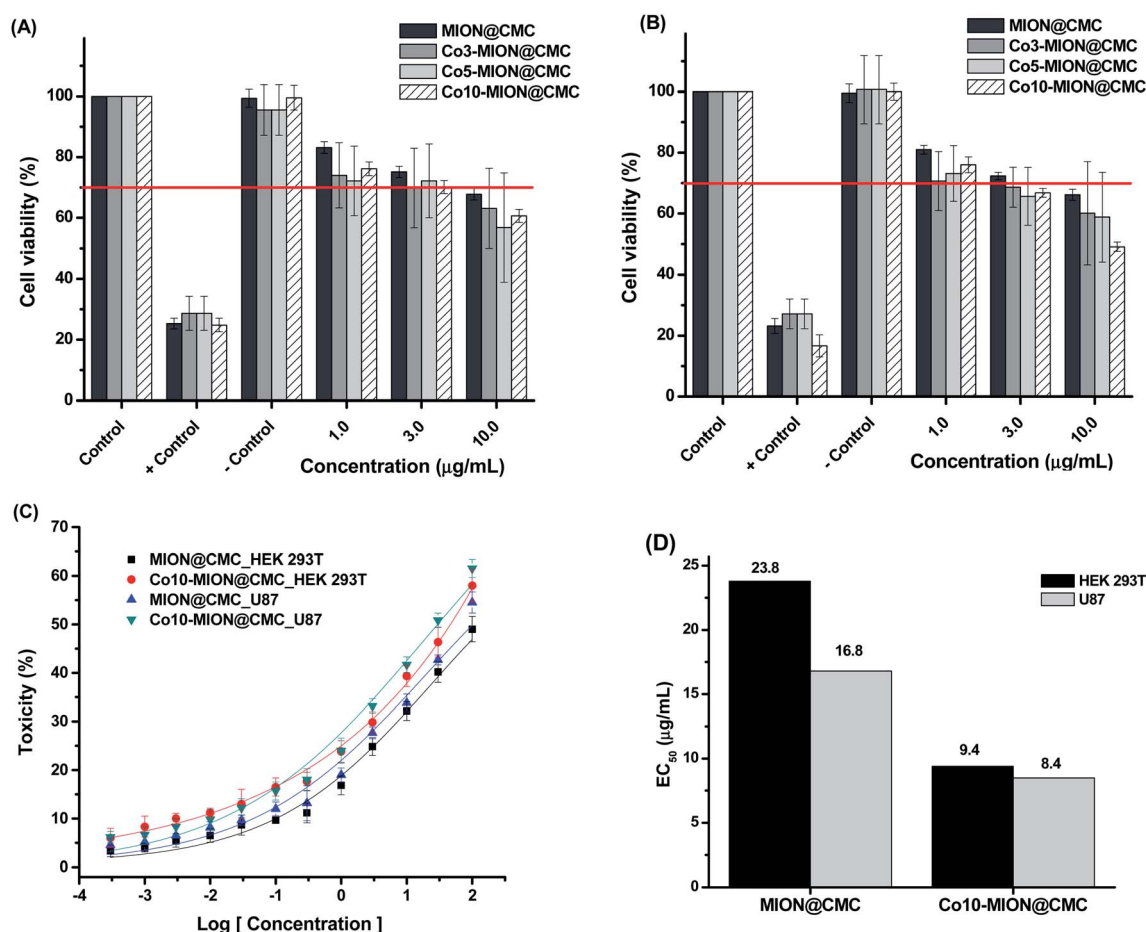


Fig. 10 MTT *in vitro* assays for normal (HEK 293T, (A)) and cancer (U87, (B)) cells incubated with MION@CMC, Co<sub>3</sub>-MION@CMC, Co<sub>5</sub>-MION@CMC, and Co<sub>10</sub>-MION@CMC nanocolloids for 24 h. (C) Dose–response curves and (D) EC<sub>50</sub> analysis ( $n = 6$ ; mean ± SD).

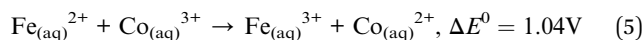
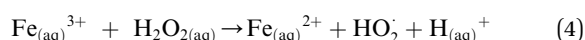
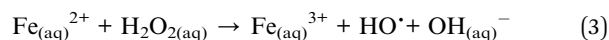
The evaluation of the relative toxicity of MION@CMC and Co<sub>10</sub>-MION@CMC was carried out using dose–response curves (Fig. 10C) and the EC<sub>50</sub> parameter (Fig. 10D). Based on the dose–

response fitted curves, the EC<sub>50</sub> values for HEK 293T and U87 cells after incubation with MION were estimated to be 23.8 µg mL<sup>-1</sup> and 16.8 µg mL<sup>-1</sup>, respectively. These values were,



however, significantly reduced to  $9.4 \mu\text{g mL}^{-1}$  and  $8.5 \mu\text{g mL}^{-1}$  after HEK 293T and U87 cells incubation with  $\text{Co}_{10}$ -MION@CMC, which evidenced the higher cytotoxicity of these Co-doped nanoconjugates.

Although an in-depth analysis of cytotoxicity mechanisms is beyond the scope of this study, a brief interpretation of the observed cell viability responses associated with iron oxide nanoparticles is presented and supported by the literature. A crucial mechanism of the toxicity of magnetite nanoparticles is the generation of reactive oxygen species (ROS). Under acidic conditions of lysosomal microenvironments, ferrous ions ( $\text{Fe}^{2+}$ ) released within the cells can react with hydrogen peroxide ( $\text{H}_2\text{O}_2$ ), leading to the production of hydroxyl radicals *via* Fenton reactions (eqn (3)). Subsequently, the  $\text{Fe}^{2+}$  species can be regenerated through the reduction of the formed ferric ions ( $\text{Fe}^{3+}$ ) by the excess of  $\text{H}_2\text{O}_2$  *via* Fenton-like reactions (eqn (4)).<sup>50,51</sup> The imbalance in the rate of ROS generation leads to oxidative stress affecting the biochemical reactions and metabolism, ultimately leading to oxidative cell death. Some studies<sup>52–54</sup> have reported that the incorporation of cobalt into magnetite nanostructure considerably enhances the peroxidase-like activity of  $\text{Fe}_3\text{O}_4$  due to the higher decomposition of hydrogen peroxide into  $\text{HO}^\cdot$  free radicals. It can be explained based on the redox potential of  $\text{Co}^{3+}/\text{Co}^{2+}$  ( $E^0 = 1.81$  V), which is higher than those of  $\text{Fe}^{3+}/\text{Fe}^{2+}$  ( $E^0 = 0.77$  V). Therefore, the reduction of  $\text{Co}^{3+}$  species by ferrous ions would be thermodynamically favorable (eqn (5)), contributing to the effective regeneration of  $\text{Co}^{2+}$  and, consequently, increased  $\text{H}_2\text{O}_2$  decomposition. Thus, the overproduction of ROS induces oxidative stress that can cause cell damage and even cell death.<sup>55,56</sup> Additionally, other studies<sup>57,58</sup> reported that the toxicity of spinel ferrites changes significantly with the substitution of a transition metal. Comparing Fe and Co-based ferrites ( $\text{MFe}_2\text{O}_4$ , where  $\text{M} = \text{Fe}$  or  $\text{Co}$ ), it is suggested that Co substitution exhibit higher cytotoxic effects, corroborating our results. In summary, these cell-death events involving both MION@CMC and Co-doped MION@CMC were predominantly ascribed to the inorganic core composed of magnetite nanoparticles due to the generation of ROS.



When comparing  $\text{EC}_{50}$  values for  $\text{Co}_{10}$ -MION@CMC nanoconjugates of both cell lines (U-87 and HEK 293T, in Fig. 10D), it was observed a relative reduction of cytotoxicity towards healthy cells (*i.e.*,  $\text{EC}_{50} \sim 10\%$  higher for HEK 293T). Although statistically similar, this slight reduction of toxicity observed for healthy cells is highly desirable bearing cancer therapy applications, which can be further optimized through biofunctionalization processes using specific biomolecules (*e.g.*, folic acid, RGD-based peptides, antibodies, *etc.*) for targeting receptors overexpressed in some cancer cell membranes.<sup>49,59</sup>

The relative toxicity (Fig. 11B and C) of  $\text{Co}_{10}$ -hematite and  $\text{Co}_{10}$ -magnetite nanoparticles (Fig. 11A) was also carried out using dose–response curves (Fig. 11D) and the  $\text{EC}_{50}$  parameter (Fig. 11E). The  $\text{EC}_{50}$  values for HEK 293T and U87 cells, after incubation with  $\text{Co}_{10}$ -hematite, were estimated to be  $1973 \mu\text{g mL}^{-1}$  and  $1485 \mu\text{g mL}^{-1}$ , respectively. These values were remarkably reduced to  $6.4 \mu\text{g mL}^{-1}$  and  $9.4 \mu\text{g mL}^{-1}$  after HEK 293T and U87 cells incubation with  $\text{Co}_{10}$ -magnetite, which endorse the higher cytotoxicity of  $\text{Co}_{10}$ -MION nanoparticles. In addition, comparing  $\text{EC}_{50}$  values for Co-doped magnetite synthesized with CMC ( $\text{Co}_{10}$ -MION\_CMC) and without ligand ( $\text{Co}_{10}$ -magnetite), it was observed similar results. So, it proved that CMC, as a biocompatible polysaccharide, is non-cytotoxic and also has not significantly altered the overall cytotoxic behavior of the nanocolloids, which was ascribed to the activity of the inorganic iron oxide nanoparticle core.<sup>60</sup>

### 3.3. Magnetohyperthermia *in vitro* with glioma cancer cells

Considering the potential application of magnetic nanoparticles as active ferrofluids in inducing the death of cancer cells referred to as magneto-therapy (MHT) through heat dissipation, magnetic hyperthermia experiments were performed with glioma cells using MION@CMC and  $\text{Co}_{10}$ -MION@CMC colloidal suspensions. The selection of  $\text{Co}_{10}$ -MION@CMC was based on the higher SAR values obtained from acellular magnetic hyperthermia analyses discussed in the previous section, which is related to the efficacy of hyperthermia. On the other hand, the choice of MION@CMC was based on the absence of cobalt ions, *i.e.*, as reference MION undoped ferrofluid. Fig. 12 presented the cell viability responses of U87 cancer cells after incubation with both nanoparticles (NP) for 3 hours and exposure to the MHT assay.

For comparison, in the samples without MHT assay, it was noticed that the cell viability was reduced to approximately 70% after incubation with magnetite (MION@CMC) and Co-doped magnetite ( $\text{Co}_{10}$ -MION@CMC) nanoparticles (concentration =  $15 \mu\text{g mL}^{-1}$ ), which evidenced the intrinsic cytotoxic effect of these nanoparticles. As discussed in the previous sections and supported by the literature, this trend is associated with the concentration-dependence and time-dependence of cell viability responses towards the iron oxide-based nanomaterials assessed through MTT assay. Moreover, the cell viability response was reduced to approximately 60% and 50% when the glioma cancer cells incubated with the magnetite and Co-doped magnetite ferrofluids were exposed to the alternate magnetic field, respectively. These results demonstrated the ability of the nanoconjugates for killing cancer cells due to the local heat generated ( $\Delta T \sim +4 \text{ }^\circ\text{C}$ ) by the magnetohyperthermia process. Moreover, the results demonstrated the higher hyperthermia efficiency of  $\text{Co}_{10}$ -MION@CMC owing to the increase of magnetic anisotropy,<sup>13,38</sup> which corroborated the magnetic findings discussed in previous sections.

In summary, the nanosystems proposed based on Co-doped iron oxide nanoparticles stabilized by CMC amalgamated components and properties that are very promising regarding cancer therapy. It should be considered as a multimodal smart



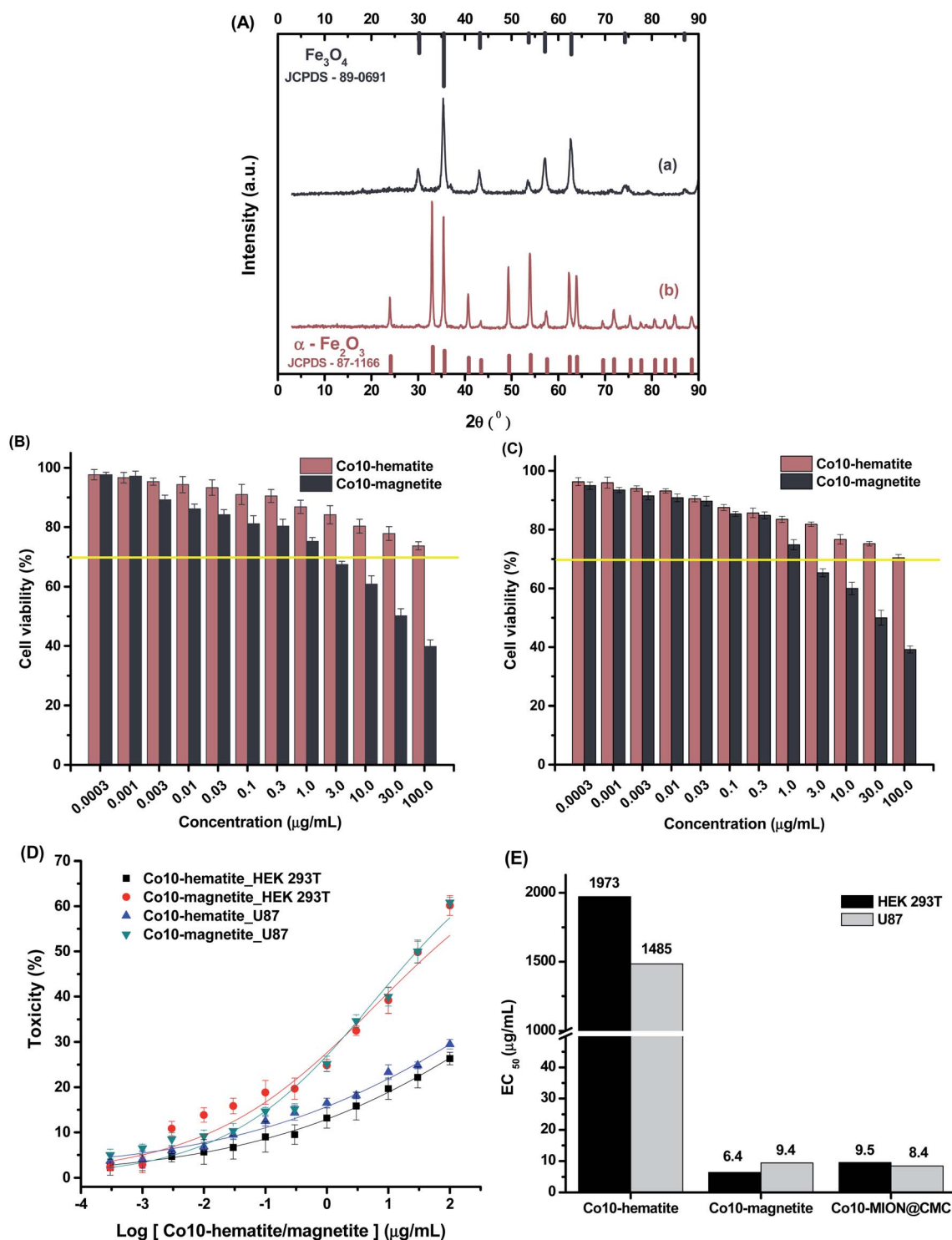


Fig. 11 (A) XRD patterns of (a) Co<sub>10</sub>-magnetite and (b) Co<sub>10</sub>-hematite powders, compared with reference patterns (Fe<sub>3</sub>O<sub>4</sub> and α-Fe<sub>2</sub>O<sub>3</sub>). MTT assays for (B) HEK 293T and (C) U87 cells incubated with Co<sub>10</sub>-magnetite and Co<sub>10</sub>-hematite nanoparticles for 24 h. (D) Dose-response curves and (E) EC<sub>50</sub> analysis ( $n = 6$ ; mean  $\pm$  SD).

nanoplatfrom for application in cancer treatment as it integrates: (a) water solubility; (b) presence of chemical functional groups in CMC for further functionalization for targeting specific tumor cells; (c) improved hyperthermia efficiency even at lower doping content at conditions below the recommended

“ $Hf$ ” value of  $5 \times 10^9 \text{ A m}^{-1} \text{ s}^{-1}$ , required for safety biomedical applications; and (d) high cytotoxicity *in vitro* associated with ROS formation that could be used in association with magnetic hyperthermia to trigger cancer cell death.



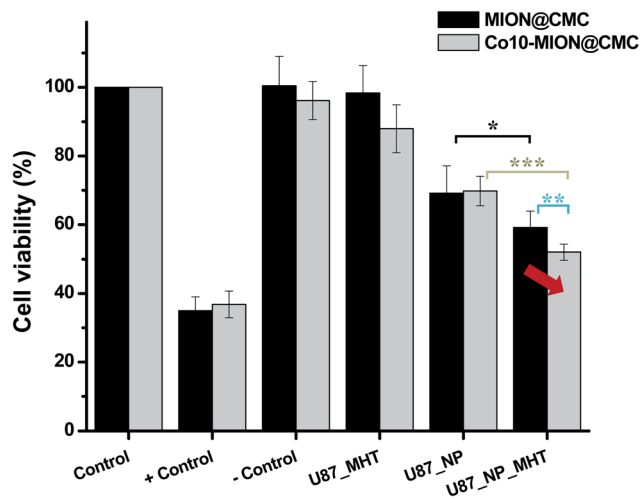


Fig. 12 Cell viability response of the U87 incubated with MION@CMC and Co<sub>10</sub>-MION@CMC systems ( $C = 15 \mu\text{g mL}^{-1}$ ) in the absence (U87-NP) and the presence of alternate magnetic field (U87-NP-MHT) ( $n = 6$ ; mean  $\pm$  SD; one-way ANOVA followed by Bonferroni's test with \* =  $p < 0.05$ ; \*\* =  $p < 0.01$ ; \*\*\* =  $p < 0.001$ . Only the significant differences were presented, excluding comparison to/between controls).

## 4. Conclusions

An eco-friendly aqueous approach based on the co-precipitation method was successfully employed for the synthesis of cobalt-doped magnetite-carboxymethylcellulose nanoconjugates. They were comprehensively characterized for their physico-chemical and magnetic properties, which were correlated with their ability to kill malignant glioblastoma cells by magnetic hyperthermia. The CMC capping ligand was responsible not only for the effective stabilization of the nanocolloids but also for tuning the magnetothermal responses under hyperthermia tests. EMR and VSM analysis confirmed that the replacement of Fe<sup>2+</sup> with Co<sup>2+</sup> (*i.e.*, 3, 5, and 10 mol%) increased the magnetocrystalline anisotropy of the systems, which in turn increased the heating rates in the acellular hyperthermia experiments. Based on the cell viability assays, the results evidenced a concentration-dependent behavior of all nanocolloids in the viability of both HEK293T and U87 cells. Furthermore, it was observed using the EC<sub>50</sub> parameter slightly higher relative cytotoxicity of Co<sub>10</sub>-MION@CMC towards cancer cells compared to healthy cells, which is highly needed for cancer therapy applications. More importantly, under an AMF, the Co<sub>10</sub>-MION@CMC nanocolloids demonstrated the highest hyperthermia efficiency owing to the increase of magnetic anisotropy. In view of these examinations, the cobalt doping may represent a valuable strategy to improve the magnetic hyperthermia performance of very small (~7–8 nm) iron oxide nanoparticles for applications in multimodal cancer therapy.

## Author's contribution

Alice G. Leonel: conceptualization, methodology, visualization, investigation, formal analysis, writing – original draft, writing –

review & editing. Alexandra A. P. Mansur: conceptualization, methodology, visualization, investigation, formal analysis, writing – original draft, writing – review & editing. Sandhra M. Carvalho: methodology, visualization, investigation, formal analysis, writing – original draft, writing – review & editing. Luis Eugenio F. Outon: methodology, visualization, investigation, formal analysis, writing – original draft, writing – review & editing. José Domingos Ardisson: methodology, visualization, investigation, formal analysis, writing – original draft, writing – review & editing, resources. Klaus Krambrock: methodology, visualization, validation, funding acquisition, writing – original draft, writing – review & editing, resources. Herman S. Mansur: supervision, conceptualization, methodology, visualization, validation, funding acquisition, writing – original draft, writing – review & editing, resources, project administration.

## Funding sources

The financial support of this work was provided by the following Brazilian research agencies: CAPES – Coordenação de Aperfeiçoamento de Pessoal de Nível Superior (PNPD; PROINFRA2010–2014; PROEX-2020); FAPEMIG – Fundação de Amparo à Pesquisa do Estado de Minas Gerais (PPM-00760-16; UNIVERSAL-APQ-00291-18); CNPq – Conselho Nacional de Desenvolvimento Científico e Tecnológico (PQ1A-303893/2018-4; UNIVERSAL-457537/2014-0; 421312/2018-1; PIBIC-2017/2018/2019); and FINEP – Financiadora de Estudos e Projetos (CTINFRA-PROINFRA 2008/2010/2011/2018); UFMG/PRPq.

## Conflicts of interest

The authors declare no competing interest regarding the publication of this paper.

## Acknowledgements

The authors acknowledge the staff of the Center of Nanoscience, Nanotechnology and Innovation – CeNano<sup>2</sup> I/CEMUCASI/UFMG for spectroscopy analyses. Also, the authors express their gratitude to the staff at the Microscopy Center at UFMG for their assistance with TEM analysis.

## References

- 1 E. Myrovali, N. Maniotis, A. Makridis, A. Terzopoulou, V. Ntomprougkidis, K. Simeonidis, D. Sakellari, O. Kalogirou, T. Samaras, R. Salikhov, M. Spasova, M. Farle, U. Wiedwald and M. Angelakeris, *Sci. Rep.*, 2016, **6**, 1–11.
- 2 M. P. Calatayud, E. Soler, T. E. Torres, E. Campos-Gonzalez, C. Junquera, M. R. Ibarra and G. F. Goya, *Sci. Rep.*, 2017, **7**, 1–16.
- 3 S. Ahmed, B. L. Rajak, M. Gogoi and H. D. Sarma, in *Smart Healthcare for Disease Diagnosis and Prevention*, Elsevier Inc., 2020, pp. 153–173.
- 4 Y. Hadadian, A. P. Ramos and T. Z. Pavan, *Sci. Rep.*, 2019, **9**, 1–14.





- 5 A. Sathya, P. Guardia, R. Brescia, N. Silvestri, G. Pugliese, S. Nitti, L. Manna and T. Pellegrino, *Chem. Mater.*, 2016, **28**, 1769–1780.
- 6 R. Moreno, S. Poyser, D. Meilak, A. Meo, S. Jenkins, V. K. Lazarov, G. Vallejo-Fernandez, S. Majetich and R. F. L. Evans, *Sci. Rep.*, 2020, **10**, 2722–2732.
- 7 S. Nappini, E. Magnano, F. Bondino, I. Piš, A. Barla, E. Fantechi, F. Pineider, C. Sangregorio, L. Vaccari, L. Venturelli and P. Baglioni, *J. Phys. Chem. C*, 2015, **119**, 25529–25541.
- 8 B. Sivakumar, R. G. Aswathy, Y. Nagaoka, M. Suzuki, T. Fukuda, Y. Yoshida, T. Maekawa and D. N. Sakthikumar, *Langmuir*, 2013, **29**, 3453–3466.
- 9 A. Aravamudhan, D. M. Ramos, A. A. Nada and S. G. Kumbar, in *Natural and Synthetic Biomedical Polymers*, Elsevier Inc., 2014, pp. 67–89.
- 10 G. Aguilera, C. C. Berry, R. M. West, E. Gonzalez-Monterrubio, A. Angulo-Molina, Ó. Arias-Carrión and M. Á. Méndez-Rojas, *Nanoscale Adv*, 2018, **1**, 671–685.
- 11 S. M. Carvalho, A. G. Leonel, A. A. P. Mansur, I. C. Carvalho, K. Krambrock and H. S. Mansur, *Biomater. Sci.*, 2019, **7**, 2102–2122.
- 12 S. Laurent, S. Dutz, U. O. Häfeli and M. Mahmoudi, *Adv. Colloid Interface Sci.*, 2011, **166**, 8–23.
- 13 E. Fantechi, C. Innocenti, M. Albino, E. Lottini and C. Sangregorio, *J. Magn. Magn. Mater.*, 2015, 365–371.
- 14 Y. Luengo, M. A. Roldan, M. Varela, F. Herranz, M. P. Morales and S. Veintemillas-Verdaguer, *J. Phys. Chem. C*, 2019, **123**, 7356–7365.
- 15 A. G. Leonel, H. S. Mansur, A. A. P. Mansur, A. Caires, S. M. Carvalho, K. Krambrock, L. E. F. Outon and J. D. Ardisson, *Int. J. Biol. Macromol.*, 2019, **132**, 677–691.
- 16 O. L. Lanier, O. I. Korotych, A. G. Monsalve, D. Wable, S. Savliwala, N. W. F. Grooms, C. Nacea, O. R. Tuitt and J. Dobson, *Int. J. Hyperthermia*, 2019, **36**, 686–700.
- 17 S. Anjum, R. Tufail, K. Rashid, R. Zia and S. Riaz, *J. Magn. Magn. Mater.*, 2017, **432**, 198–207.
- 18 M. A. Ahmed, N. Okasha and S. I. El-Dek, *Ceram. Int.*, 2010, **36**, 1529–1533.
- 19 J. M. Byrne, V. S. Coker, S. Moise, P. L. Wincott, D. J. Vaughan, F. Tuna, E. Arenholz, G. Van Der Laan, R. A. D. Patrick, J. R. Lloyd and N. D. Telling, *Interface*, 2013, **10**, 1–12.
- 20 C. F. Holder and R. E. Schaak, *ACS Nano*, 2019, **13**, 7359–7365.
- 21 T. Fujii, F. M. F. de Groot, G. A. Sawatzky, F. C. Voogt, T. Hibma and K. Okada, *Phys. Rev. B: Condens. Matter Mater. Phys.*, 1999, **59**, 3195–3202.
- 22 H. Liu, G. Wei, Z. Xu, P. Liu and Y. Li, *Appl. Surf. Sci.*, 2016, **389**, 438–446.
- 23 M. I. Dar and S. A. Shivashankar, *RSC Adv.*, 2014, **4**, 4105–4113.
- 24 P. X. Sheng, Y.-P. Ting, J. P. Chen and L. Hong, *J. Colloid Interface Sci.*, 2004, **275**, 131–141.
- 25 A. A. P. Mansur, F. G. De Carvalho, R. L. Mansur, S. M. Carvalho, L. Carlos, D. Oliveira and H. S. Mansur, *Int. J. Biol. Macromol.*, 2017, **96**, 675–686.
- 26 Z. E. Gahrouei, S. Labbaf and A. Kermanpur, *Phys. E*, 2020, **116**, 113759–113772.
- 27 V. S. Kumbhar, A. D. Jagadale, N. M. Shinde and C. D. Lokhande, *Appl. Surf. Sci.*, 2012, **259**, 39–43.
- 28 B. J. Rani, M. Ravina, B. Saravanakumar, G. Ravi, V. Ganesh, S. Ravichandran and R. Yuvakkumar, *Nano-Struct. Nano-Objects*, 2018, **14**, 84–91.
- 29 M. G. Carneiro-Da-Cunha, M. A. Cerqueira, B. W. S. Souza, J. A. Teixeira and A. A. Vicente, *Carbohydr. Polym.*, 2011, **85**, 522–528.
- 30 S. Bhattacharjee, *J. Control. Release*, 2016, **235**, 337–351.
- 31 E. Buhler and M. Rinaudo, *Macromolecules*, 2000, **33**, 2098–2106.
- 32 V. Singh and V. Banerjee, *J. Appl. Phys.*, 2012, **112**, 1–10.
- 33 T. E. Torres, E. Lima, M. P. Calatayud, B. Sanz, A. Ibarra, R. Fernández-Pacheco, A. Mayoral, C. Marquina, M. R. Ibarra and G. F. Goya, *Sci. Rep.*, 2019, **9**, 3992–4001.
- 34 C. Naud, C. Thebault, M. Carrière, Y. Hou, R. Morel, F. Berger, B. Dieny and H. Joisten, *Nanoscale Adv*, 2020, **2**, 3632–3655.
- 35 G. Iglesias, A. V. Delgado, M. Kujda and M. M. Ramos-Tejada, *Colloid Polym. Sci.*, 2016, **294**, 1541–1550.
- 36 M. Sanna Angotzi, V. Mameli, C. Cara, A. Musinu, C. Sangregorio, D. Niznansky, H. L. Xin, J. Vejpravova and C. Cannas, *Nanoscale Adv*, 2020, **2**, 3191–3201.
- 37 O. Rahman, S. C. Mohapatra and S. Ahmad, *Mater. Chem. Phys.*, 2012, **132**, 196–202.
- 38 F. L. Deepak, M. Bañobre-López, E. Carbo-Argibay, M. F. Cerqueira, Y. Piñeiro-Redondo, J. Rivas, C. M. Thompson, S. Kamali, C. Rodriguez-Abreu, K. Kovnir and Y. V. Kolen'ko, *J. Phys. Chem.*, 2015, **119**, 11947–11957.
- 39 I. Sharifi, H. Shokrollahi and S. Amiri, *J. Magn. Magn. Mater.*, 2012, **324**, 903–915.
- 40 Y. Piñeiro-Redondo, M. Bañobre-López, I. Pardiñas-Blanco, G. Goya, M. A. López-Quintela and J. Rivas, *Nanoscale Res. Lett.*, 2011, **6**, 1–7.
- 41 M. M. Noginova, N. Noginova, O. Amponsah, R. Bah, R. Rakhimov and V. A. Atsarkin, *J. Magn. Magn. Mater.*, 2008, **320**, 2228–2232.
- 42 C. Iacovita, I. Fizean, A. Pop, L. Scorus, R. Dudric, G. Stiufluic, N. Vedeau, R. Teteau, F. Loghin, R. Stiufluic and C. M. Lucaciu, *Pharmaceutics*, 2020, **12**, 1–25.
- 43 G. Barrera, P. Tiberto, P. Allia, B. Bonelli, S. Esposito, A. Marocco, M. Pansini and Y. Leterrier, *Appl. Sci.*, 2019, **9**, 212–240.
- 44 R. Tackett, C. Sudakar, R. Naik, G. Lawes, C. Rablau and P. P. Vaishnav, *J. Magn. Magn. Mater.*, 2008, **320**, 2755–2759.
- 45 Q. Song and Z. John Zhang, *J. Phys. Chem. B*, 2006, **110**, 11205–11209.
- 46 S. K. Sharma, N. Shrivastava, F. Rossi, L. D. Tung and N. T. K. Thanh, *Nano Today*, 2019, **19**, 100795.
- 47 F. Soetaert, S. K. Kandala, A. Bakuzis and R. Ivkov, *Sci. Rep.*, 2017, **7**, 6661.
- 48 C. Buzea and I. Pacheco, in *Nanotechnology in Eco-efficient Construction*, Elsevier Ltd, 2019, pp. 705–754.



- 49 A. A. P. Mansur, H. S. Mansur, A. G. Leonel, I. C. Carvarlho, M. C. G. Lage, S. M. Carvalho, K. Krambrock and Z. I. P. Lobato, *J. Mater. Chem. B*, 2020, **8**, 7166–7188.
- 50 B. Wang, J. J. Yin, X. Zhou, I. Kurash, Z. Chai, Y. Zhao and W. Feng, *J. Phys. Chem. C*, 2013, **117**, 383–392.
- 51 P. P. Fu, Q. Xia, H. M. Hwang, P. C. Ray and H. Yu, *J. Food Drug Anal.*, 2014, **22**, 64–75.
- 52 R. C. C. Costa, M. De Fátima Fontes Lelis, L. C. A. Oliveira, J. D. Fabris, J. D. Ardisson, R. R. V. A. Rios, C. N. Silva and R. M. Lago, *Catal. Commun.*, 2003, **4**, 525–529.
- 53 R. Alrozi, N. Aida Zubir, M. Khairul Azam Selamat, A. Nurzalikha Zakarya and N. Syaherra Paisan, *Mater. Today Proc.*, 2018, **5**, 21874–21878.
- 54 Y. Zhu, R. Zhu, Y. Xi, J. Zhu, G. Zhu and H. He, *Appl. Catal. B Environ.*, 2019, **255**, 117739–117755.
- 55 M. Ahamed, M. J. Akhtar, M. A. M. Khan, H. A. Alhadlaq and A. Alshamsan, *Colloids Surf., B*, 2016, **148**, 665–673.
- 56 M. J. Akhtar, M. Ahamed, H. A. Alhadlaq and A. Alshamsan, *Toxicol. Vitro*, 2017, **40**, 94–101.
- 57 H. Zhao, Z. Chen, L. Tao, X. Zhu, M. Lan and Z. Li, *RSC Adv.*, 2015, **5**, 68454–68460.
- 58 F. Ahmad and Y. Zhou, *Chem. Res. Toxicol.*, 2017, **30**, 492–507.
- 59 A. A. P. Mansur, S. M. Carvalho, Z. I. P. Lobato, M. D. F. Leite, A. D. S. Cunha and H. S. Mansur, *Bioconjug. Chem.*, 2018, **29**, 1973–2000.
- 60 A. G. Leonel, A. A. P. Mansur and H. S. Mansur, *Water Res.*, 2021, **190**, 116693.

